ISSN 8755-6839

SCIENCE OF TSUNAMI HAZARDS

The International Journal of The Tsunami Society

Volume 26 Number 1 Published Electronically 2007

THE TSUNAMI SOCIETY
P. O. Box 2117
Ewa Beach, HI 96706-0117, USA

WWW.TSUNAMISOCIETY.ORG

OBJECTIVE: The Tsunami Society publishes this journal to increase and disseminate knowledge about tsunamis and their hazards.

DISCLAIMER: Although these articles have been technically reviewed by peers, The Tsunami Society is not responsible for the veracity of any statement, opinion or consequences.

Submit manuscripts of articles, notes or letters to the Editor. If an article is accepted for publication the author(s) must submit a scan ready manuscript, a Doc, TeX or a PDF file in the journal format. Issues of the journal are published electronically in PDF format. Recent journal issues are available at:
http://www.TsunamiSociety.org
and at http://www.sthjournal.org

Tsunami Society members will be advised by e-mail when a new issue is available. There are no page charges for one paper per calendar year for authors who are members of the Tsunami Society. Permission to use figures, tables and brief excerpts from this journal inscientific and educational works is hereby granted provided that the source is acknowledged.

Issues of the journal from 1982 thru 2005 are available in PDF format at
http://epubs.lanl.gov/tsunami/ and on a CD-ROM from the Society to Tsunami Society members.
ISSN 8755-6839 http://www.sthjournal.org

Published Electronically by The Tsunami Society in Honolulu, Hawaii, USA

PRELIMINARY ANALYSIS OF THE EARTHQUAKE (MW 8.1) AND TSUNAMI OF APRIL 1, 2007, IN THE SOLOMON ISLANDS, SOUTHWESTERN PACIFIC OCEAN

Michael A. Fisher, Eric L. Geist, Ray Sliter, Florence L. Wong, Carol Reiss, and Dennis M. Mann

U.S. Geological Survey,
345 Middlefield Rd., MS 999, Menlo Park, California, USA

ABSTRACT

On April 1, 2007, a destructive earthquake (Mw 8.1) and tsunami struck the central Solomon Islands arc in the southwestern Pacific Ocean. The earthquake had a thrust-fault focal mechanism and occurred at shallow depth (between 15 km and 25 km) beneath the island arc. The combined effects of the earthquake and tsunami caused dozens of fatalities and thousands remain without shelter. We present a preliminary analysis of the Mw-8.1 earthquake and resulting tsunami. Multichannel seismic-reflection data collected during 1984 show the geologic structure of the arc's frontal prism within the earthquake's rupture zone. Modeling tsunami-wave propagation indicates that some of the islands are so close to the earthquake epicenter that they were hard hit by tsunami waves as soon as 5 min. after shaking began, allowing people scant time to react.

1. INTRODUCTION

The M-8.1 earthquake in the Solomon Islands that occurred at 20:40 on April 1, 2007 (UTC), struck along a complicated plate boundary in the southwestern Pacific Ocean (Figure 1). Earthquake shaking and a tsunami caused as many as 52 fatalities and left thousands homeless (Reliefweb, 2007a). These figures remain unconfirmed because the affected area is impoverished and remote from government resources. Clearly, however, this earthquake's aftermath includes considerable human suffering.

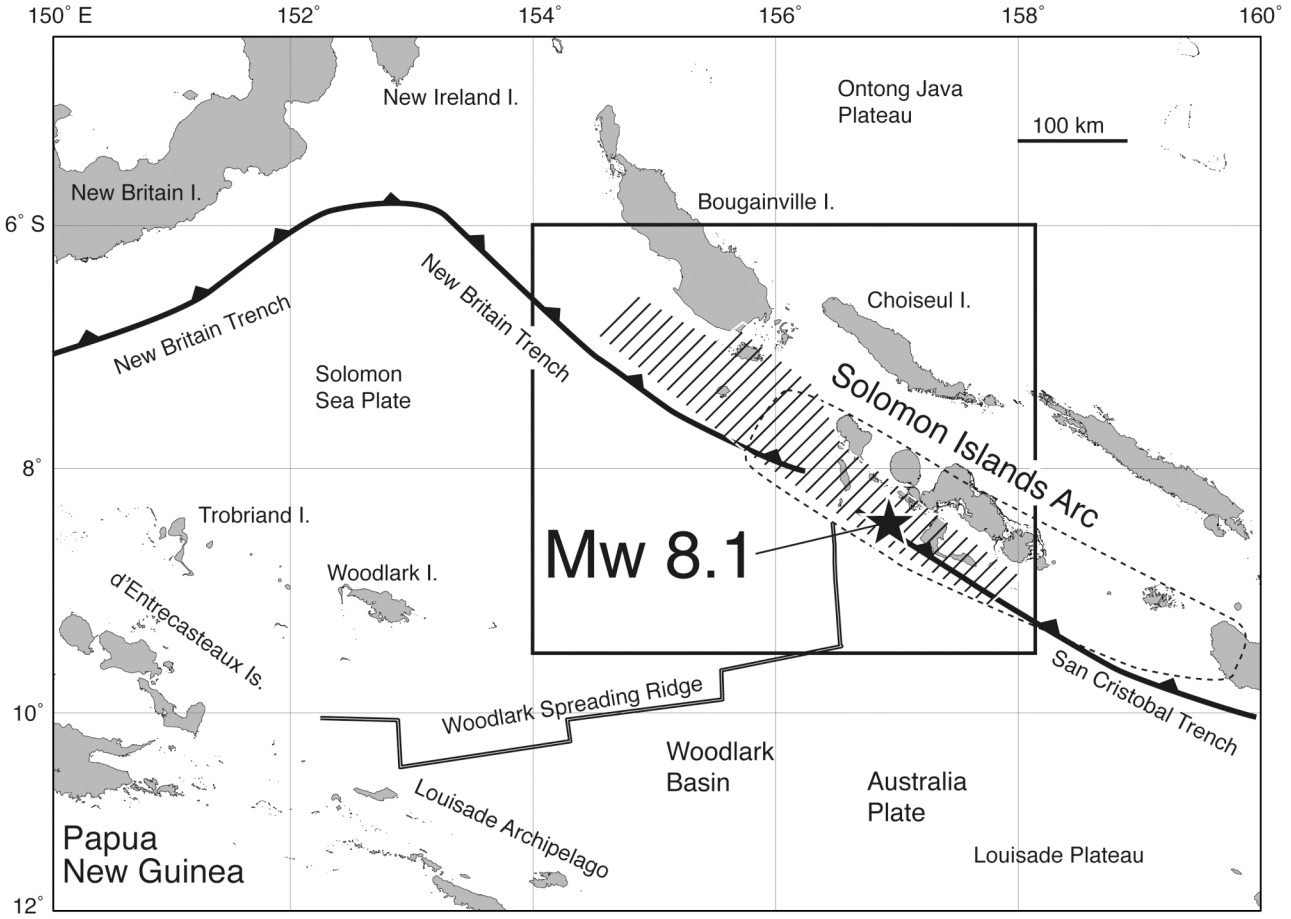

Figure 1. Index map of the part of the southwest Pacific Ocean that includes the Solomon Islands arc and the epicenter of the 2007 Mw-8.1 subduction-zone earthquake. The crosshatched area shows the rupture zone of the 2007 earthquake. The dotted outline shows the part of the island arc that has been characterized by a reduced level of historical seismicity (Cooper and Taylor, 1987). The box shows the area included in Figure 2a. Plate-convergence rates and directions are from Mann et al. (1998).

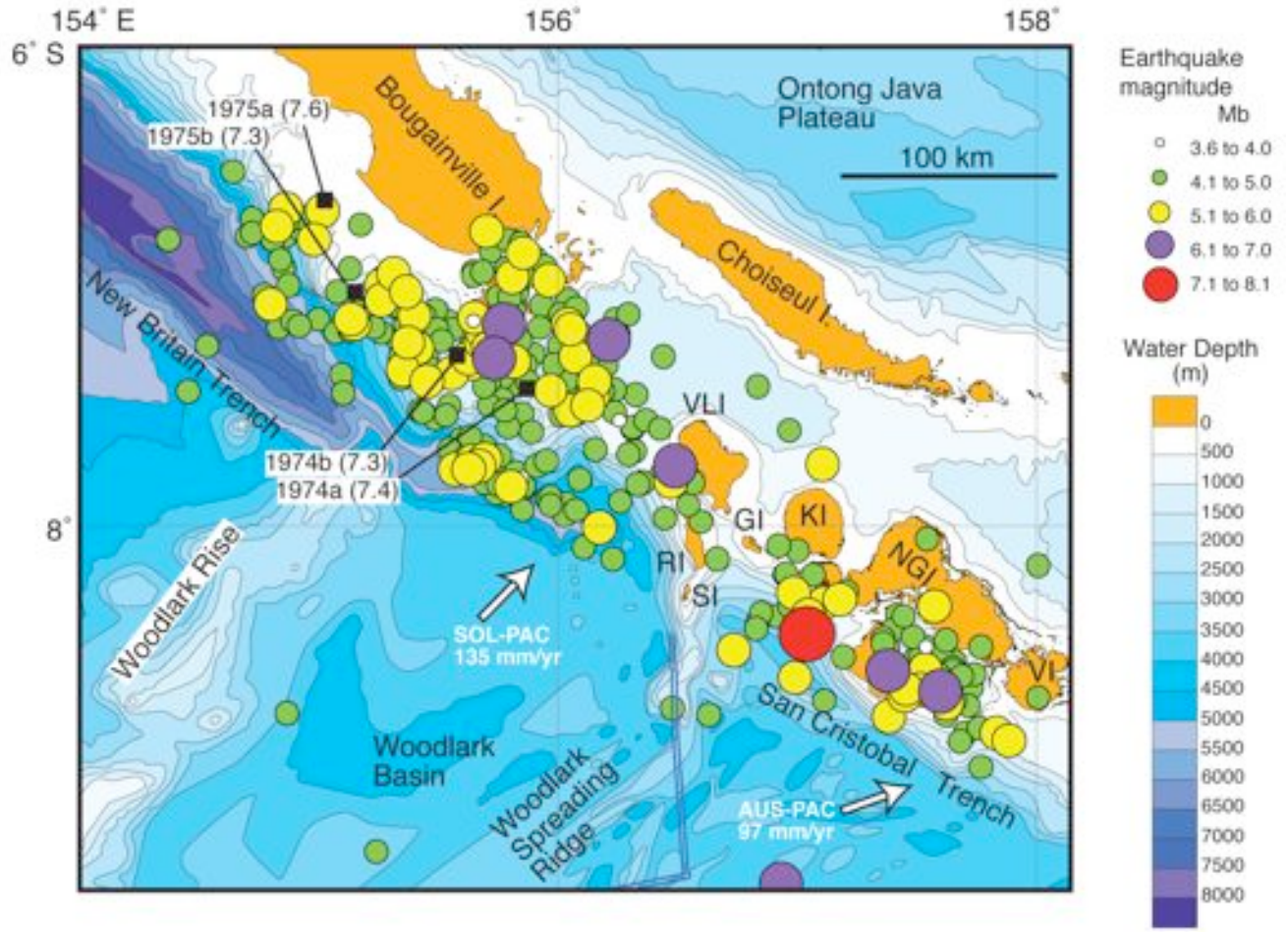

Figure 2a. Location of main shock (red circle) and aftershocks of the 2007 Mw-8.1 earthquake. Plate-convergence rates and directions are from Mann et al. (1998). Black squares and numbers like "1975a (7.6) " give year, sequence and magnitude of doublet earthquakes that occurred in the rupture zone of the 2007 earthquake. Figure area given in Figure 1. GI: Ghizo Island. KI: Kolombangara Island. NBT: New Britain Trench. NGI: New Georgia Island. RI: Ranongga Island. SCT: San Cristobol Trench. SI: Simbo Island. VI: Vangunu Island: VLI: Vela Lavella Island.

The Solomon Islands arc lies along the southwestern boundary of the Pacific plate, and the Mw-8.1 earthquake was a subduction-zone thrust event. Several aspects of geography and geology make this earthquake and tsunami unique. First, although young oceanic crust is being subducted eastward at the New Britain Trench, the down going plate bends sharply downward and dips steeply (30˚ to 45˚) into the mantle, and the earthquake's epicenter is located almost beneath the trench axis (Figure 2a). Second, in the past 30 years, numerous earthquake doublets have struck this island arc (e.g. Lay and Kanamori, 1980), and the rupture zone of the 2007 earthquake includes the locations of two doublets, having magnitudes of about M 7 (Figure 2a). To date (9/1/2007), however, the 2007 event has produced aftershocks as large as Mb 6.6, but no second M-8 earthquake and tsunami have occurred.

Third, where the earthquake struck, complex bathymetric and tectonic elements, including an active spreading ridge and transform fault, are being subducted. The effect of ridge subduction on seismogenesis is evident from the fact that earthquake slip began southeast of where the spreading ridge enters the subduction zone; slip was reduced directly over the ridge; and northwest of the ridge, slip resumed with increased amplitude.

2. GEOLOGIC SETTING OF THE EPICENTRAL REGION

Since the middle Miocene, the Ontong Java Plateau (Figure 1) has been colliding with the trench along the east side of the Solomon Islands arc (Kroenke, 1972; Mann and Taira, 2004; Phinney et al., 1999). This collision caused eastward subduction of oceanic crust to commence along the west side of the arc, forming an exemplar of subduction-polarity reversal (e.g. Karig and Mammerickx, 1972). Earthquake hypocenters indicate that oceanic crust on both the east and the west sides of the island arc is being subducted (e.g. Cooper and Taylor, 1985, 1987; Shinohara et al., 2003; Yoneshima et al., 2005).

The 2007 Mw-8.1 earthquake occurred along the west side of the arc, where the New Britain and San Cristobal Trenches mark the northeastward subduction of the oceanic plates on the west. This crust includes the Solomon Sea plate to the north and the Australia plate to the south across the Woodlark spreading ridge (Figure 1). Plate convergence between the Solomon Sea and Pacific plates, is rapid, amounting to about 100 mm/yr (Bird, 2003; Tregoning et al., 1998).

The Woodlark spreading ridge extends discontinuously eastward across the Woodlark Basin to where the ridge is being underthrust at the New Britain Trench, along the west side of the Solomon Islands arc (Goodliffe, et al., 1999; Martinez, et al., 1999; Taylor, 1999; Taylor and Exon, 1987; Weissel et al., 1982)(Figure 1). The spreading ridge figures prominently in this study because the ridge enters the trench only about 50 km northwest of the epicenter for the 2007 earthquake (Figure 2b). North of the Woodlark spreading ridge, the New Britain Trench deepens northwestward, from about 5 km near the ridge to as deep as 8 km west of Bougainville Island (Figure 1 and 2a). Across the spreading ridge to the southeast, the San Cristobal trench is not well expressed bathymetrically, at depths of 4 km to 5 km.

The Woodlark spreading ridge became active about 6 Ma ago (Taylor et al., 1999), and modeling geodetic data indicates that the current half-spreading rate across the ridge increases progressively eastward toward the New Britain Trench, where the half-rate may be as much as 40 mm/yr (Tregoning et al., 1998).

This spreading ridge is segmented by several transform faults (e.g. Martinez et al., 1999; Taylor et al., 1999). In particular, near the New Britain Trench the Simbo transform fault extends northward from a spreading-ridge segment (Figure 2b) to obliquely underthrust the arc's frontal prism. Swath-bathymetric data indicate that the transform fault widens northeastward, which has been interpreted as evidence for crustal spreading along this transform fault since about 80 ka (Martinez et al., 1999).

Ghizo Ridge, possibly an extinct segment of the spreading-ridge, is surmounted by seamounts and extends southeastward along the axis of the San Cristobal Trench (Figure 2b). The epicenter of the 2007 earthquake is located just northeast of Ghizo Ridge and within a re-entrant in the forearc slope.

The Simbo bathymetric ridge, distinct from the transform fault, extends northward across the

forearc slope and supports Simbo and Ranongga Islands (Figure 2b). These islands are near the trench axis and were among the areas hardest hit by the 2007 tsunami. Simbo Ridge and its surmounting islands apparently formed owing to subduction of the Woodlark spreading ridge. In this area, spreading-ridge subduction mainly controls the location and intensity of near-trench volcanism (e.g. Johnson et al., 1987; Taylor and Exon, 1987). Near the epicenter of the 2007 earthquake, volcanism is restricted in occurrence to the area of New Georgia Island, east of where the spreading ridge is being subducted. Near-trench volcanoes that formed Simbo Island actually lie west of the projected location of the trench axis, and other volcanoes lie within just 30 km of this axis.

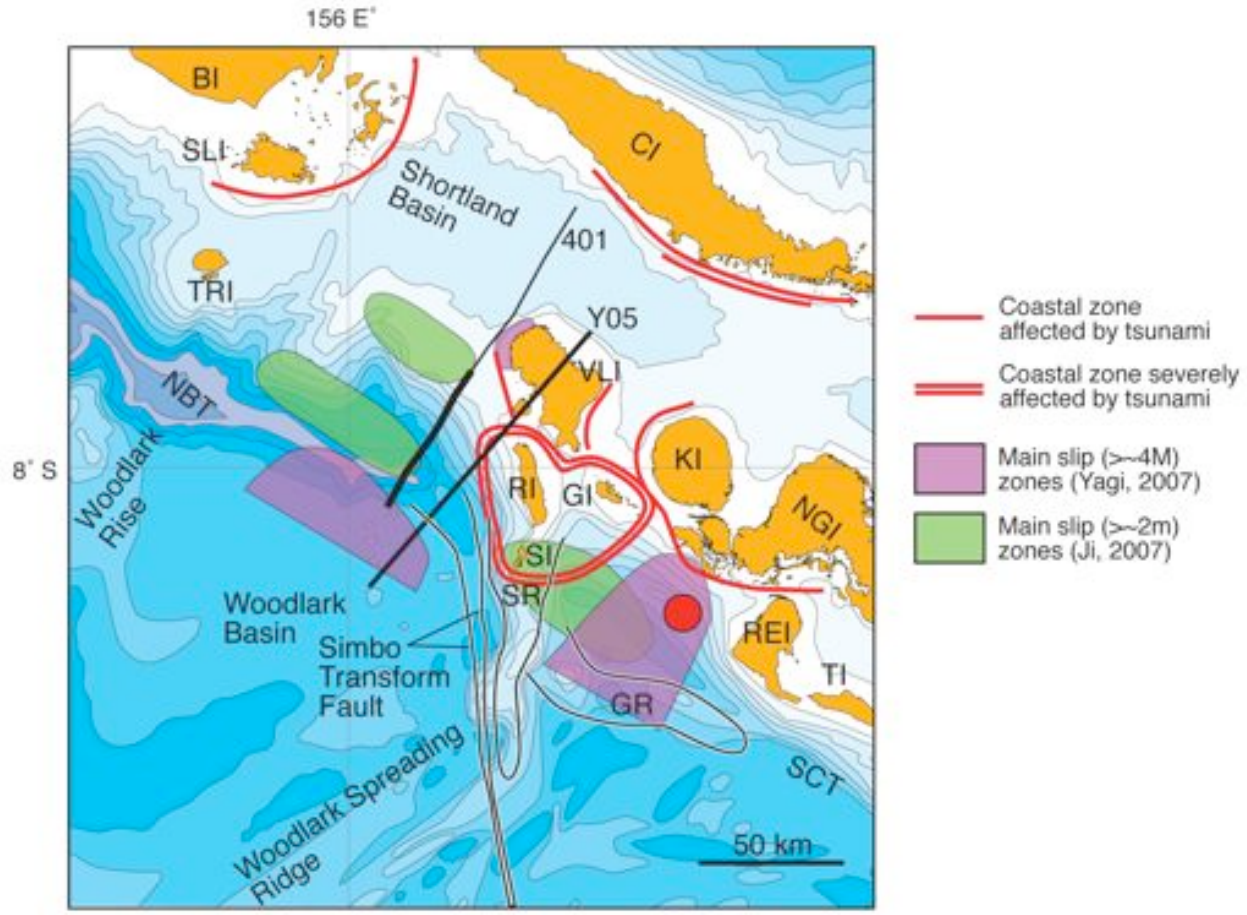

Figure 2b. The areas most severely affected by the tsunami include the near-trench islands of Simbo, Ghizo and Ranongga and the southwest coast of Choiseul Island. Red circle shows the epicenter of the 2007 Mw-8.1 earthquake. The main fault-slip zones during the 2007 earthquake are separated by the subducted Simbo transform fault. Figure area given in Figure 2a. Location of MCS section 401 in Figures 3a and 3b is shown by the heavy part of the black line labeled "401". The line of section showing locally recorded hypocenters used in Figures 3b and 3c is shown by the black line labeled "Y05". Abbreviations as in Figure 2a except for: BI: Bougainville Island. CI: Choiseul Island. GR: Ghizo ridge. REI: Rendova Island. TI: Tetepare Island. SLI: Shortland Island. SR: Simbo ridge. TRI: Treasury Island.

Another geologic consequence of ridge subduction is vertical tectonic motion of local forearc areas. For example, Mann et al. (1998) and Taylor et al. (2005) described a high spatial variation in uplift rates, near New Georgia Island, that the authors attribute to subduction of the irregular lower-plate bathymetry. The 2007 epicenter is located within a re-entrant in the lower arc slope (Figure 2b). Similar forearc re-entrants are scars caused by the subduction of high standing bathymetric features (e.g. Fisher et al., 1991; Geist et al., 1993). How tectonic processes associated with ridge subduction affected earthquake and tsunami generation are topics for further research.

3. THE 2007 EARTHQUAKE (MW 8.1)

Cooper and Taylor (1987) noted that epicenters of shallow (<70 km) and intermediate (70 km to 130 km) focal-depth earthquakes are uncommon in the central part of the island arc, as outlined in Figure 1. This central area coincides with the locus of subduction of the Woodlark spreading center (Cooper and Taylor, 1987). The epicenter for the 2007 earthquake occurred within the central zone of reduced seismicity (Figure 1), thus filling at least the northwestern half of the seismic gap.

Global CMT Catalog data (CMT, 2007) indicate that the main shock was located at 7.96˚ S and 156.40˚ E at a depth of 23 km, and the nodal plane showing thrust-fault motion strikes 331˚ and dips northeast at 38˚. Two other estimates of the attitude of the nodal plane yielded broadly similar values. According to Yagi (2007), the strike is 300˚ and the dip 19˚, whereas Ji (2007) estimated the strike to be 305˚ and dip 25˚. Fault rupture propagated northwestward from the epicenter at a mean velocity of 1.95 km/s (Yagi, 2007). The rupture zone of the 2007 earthquake extended at least 250 km along the Solomon Islands arc. Within the two-month period following the main shock, as many as 10 aftershocks with Mb between 6 and 7 had occurred.

The Solomon Islands subduction zone is noted for producing earthquake doublets--two earthquakes having similar magnitude that occur closely in space and time (Kagan and Jackson, 1999; Lay and Kanamori, 1980; Schwartz, 1999; Xu and Schwartz, 1993). The mechanism causing earthquake doublets remains controversial, although stress triggering of the second earthquake by the first one in the doublet is likely to be a significant factor. Kagan and Jackson (1999) discuss the period between doublet earthquakes.

The largest historic doublet to strike this island arc occurred 12 days apart during 1971 and involved a pair of M-8.0 and -8.1 earthquakes north of Bougainville Island (Schwartz et al., 1989). After the 2007 Mw-8.1 earthquake, despite deep concerns among disaster workers, a follow-on earthquake and tsunami have not struck.

Most earthquake doublets in the Solomon Islands have occurred north of the 2007 epicenter, in the vicinity of Bougainville Island and along the northwest-striking part of the New Britain Trench. Two doublets during 1974 and 1975 were located within the northwestern part of the 2007 rupture zone (Xu and Schwartz, 1993) (Figure 2a). The four events making up these doublets ranged in Mw from 7.3 to 7.6, and their focal mechanisms were compatible with underthrusting and subduction of the western oceanic plate. Xu and Schwartz (1993) proposed that the 1974 and 1975 doublets originated owing to the roughness of the oceanic plate that is being subducted because the Woodlark Rise enters the New Britain Trench west of the epicenters.

Subduction of high standing bathymetric features has demonstrably affected fault slip during the 2007 earthquake. According to two finite fault models (Ji, 2007; Yagi, 2007), fault rupture bridged across the subducted part of the active Woodlark spreading ridge (Figure 2b). The finite fault models differ in detail, but they agree to the extent that they show two main slip zones and a third small zone near Vella Lavella Island. However, the slip zones by Yagi (2007) are shifted southwest from, and indicate a slip magnitude nearly twice as great as, the slip zones and magnitude presented by Ji (2007). Both models indicate that one of the two main slip zones surrounded the earthquake's epicenter and that the zones are separated by an area of slip deficit located where the Woodlark spreading ridge and the Simbo transform fault are being subducted. In both models, the second or northwestern main slip zone does not extend northwest of where the Woodlark Rise enters the trench (Figure 2b), hence this bathymetric feature may have formed a barrier to earthquake rupture.

4. SEISMIC-REFLECTION SECTION THROUGH THE EARTHQUAKE RUPTURE ZONE

During 1984, the U.S. Geological Survey collected multichannel seismic-reflection (MCS) data in the Solomon Islands arc (e.g. Bruns et al., 1989b). Seismic line 401 (Figs. 3a and 3b) from this survey crosses the rupture zone of the 2007 earthquake (Figure 2b). Another version of this seismic section is shown and interpreted in Bruns et al. (1989a). For this report, we reprocessed the seismic section, migrating these data after stack and using sonobuoy-refraction velocities obtained over the lower slope and Shortland basin (Cooper et al., 1986a,b, 1989) to produce a depth section without vertical exaggeration (Figure 3b).

MCS section 401 reveals flat reflections from the interplate decollement that can be followed for more than 40 km east of the trench (Figure 3a). These events separate discontinuous and weak reflections from within the superjacent frontal prism of the island arc from more continuous reflections from lower-plate rocks. The time and the depth-converted MCS sections (Figs. 3a and 3b) reveal rocks under the decollement that dip consistently southeastward and terminate against the abrupt seafloor rise that borders the New Britain Trench on the southeast. This rise is located along the Simbo transform fault. Swath bathymetry shows that this transform fault strikes north, nearly perpendicular to the seismic section, and the fault widens toward the New Britain Trench (Martinez et al., 1998) (Figure 2b). Lower-plate rocks that dip southeast and abut the transform fault appear to fill a half graben (Figs. 3a and 3b). This half graben may have resulted from the crustal spreading along this transform fault that occurred since about 80 ka (Martinez et al., 1999), but the graben fill may be too thick (~2 km) to have resulted solely from such a short period of extension. Alternatively, the velocity used in the depth conversion is wrong and exaggerates the thickness.

To estimate the location of the interplate boundary northwest of where reflections from the decollement end on MCS section 401, we plotted locally recorded hypocenters, instead of teleseismically located ones, on the depth section (Figure 3b) and on a regional cross section (Figure 3c). The local hypocenters were determined from data obtained during a deployment of ocean-bottom seismometers in 1998 (Yoneshima et al. 2005). Yoneshima et al. (2005) used these hypocenters to show that the seismic front underlies the upper slope, consistently below the 1000 m isobath, and that the down going plate dips ~30˚ northeast through the zone of highest seismic activity, which is deeper than about 20 km. The water bottom multiple on MCS section 401 becomes a wide band of persistent

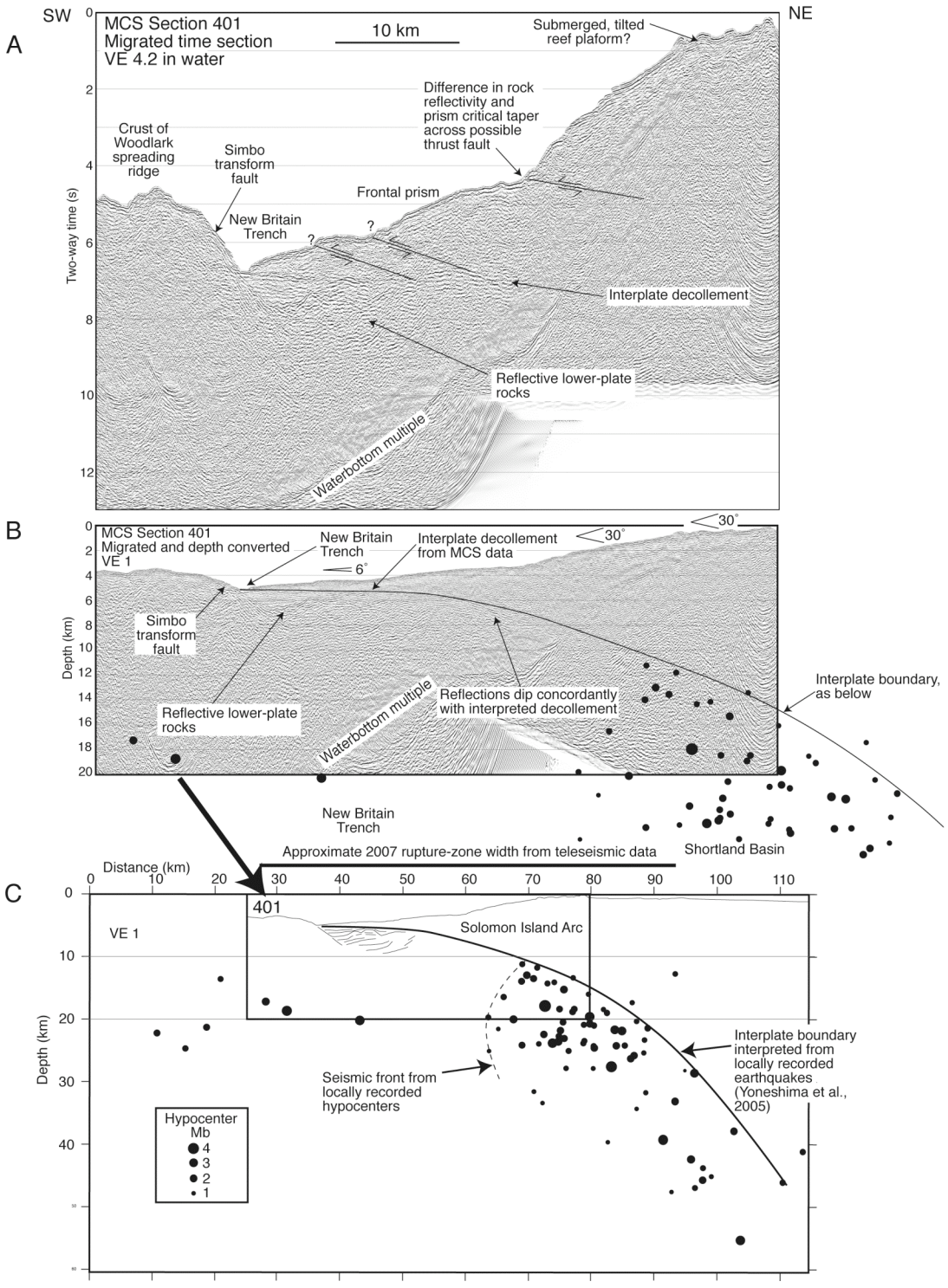

Figure 3a. Migrated time section of U.S. Geological Survey seismic line. Section location shown in Figure 2b by the black line annotated “401”.

noise when migrated (Figure 3a), and it prevents us from making a direct connection between the decollement indicated by reflections and the interplate boundary indicated by hypocenters.

Three seafloor discontinuities over the frontal prism may signify active thrust faults (Figs. 3a and 3b). The two discontinuities closer to the trench occur where reflections from within the prism are poor, so the faults are speculative. However, reflections from near the shallowest seafloor discontinuity yield better evidence for a thrust fault in that rocks at shallow depth on the fault's upslope side are more reflective and thicker than are rocks on the down slope side. Recent research interest has focused on the role in tsunamigenesis played by splay thrust faults that deform a frontal prism, especially in studies conducted off the Nankai Trough (e.g. Bangs et al., 2004; Kondo et al., 2005; Park et al., 2000, 2002). Concerning the 2007 earthquake in the Solomon Islands, we currently lack sufficient information to determine whether thrust faults interpreted from MCS section 401 (Figs. 3a and 3b) were active during the earthquake, but their potential role is a topic for future research.

The shallowest interpreted thrust fault coincides with an abrupt change in the critical taper of the wedge (Figs. 3a and 3b). Over the lowermost slope, the wedge critical taper is 6˚ whereas at the shallowest fault, the taper increases to 30˚, and the taper maintains this value eastward to beyond the shelf break (Figure 3b). At other subduction zones, variations in the critical taper of the frontal prism provide clues to how and where major earthquakes might nucleate along an interplate decollement (Wang and Hu, 2006; Kimura et al., 2007). Furthermore, Kimura et al. (2007) discuss the Nankai accretionary prism and link variations in critical wedge taper to specific structural styles within the wedge and to mechanical properties along the decollement. In the analysis by Wang and Hu (2006) the break in slope between a forearc basin and the outboard accretionary prism coincides with the outward-directed change in frictional properties along the decollement from velocity-weakening to velocity-strengthening. Hence, in this analysis the slope break is proposed to overlie the updip end of the seismogenic zone.

These findings are difficult to apply straightforwardly to the case of the Solomon Islands arc near MCS line 401 because the nearby subduction of the Woodlark spreading ridge, with its irregular bathymetry and probable high heat flow, injects a strongly three-dimensional aspect into the analysis. However, the half graben associated with the Simbo transform fault thins northeastward and appears to die out altogether below the increase in critical taper (Figure 3a). Thus the critical-taper increase from 6˚ to 30˚ may coincide with a change in frictional properties across the decollement: presumably northwest of where the graben ends, lower-plate rocks just under the decollement are igneous oceanic crust instead of sedimentary graben fill. This lithologic change might form the updip limit of the seismogenic zone.

The seismic section shows what may be pinnacle reefs under shallow water near the shelf break (Figure 3a). If they are reefs, then their flat upper surfaces indicate previous sea levels and the present depth of the pinnacles indicates submergence and southeastward tilting of the shelf edge. This may be evidence for subduction erosion of the upper plate by high standing bathymetric features thrust beneath the island arc.

5. THE TSUNAMI

According to news reports, the areas most severely affected by tsunami inundation include the near-trench islands of Simbo, Ranongga, and especially Ghizo (e.g. Unosat, 2007) as well as the southwest coast of Choiseul Island, which lies east of the Shortland Basin (Figure 2b). Reportedly, the tsunami waves were between two and ten meters high and swept inland for almost half a kilometer (Alertnet, 2007). Thirty-three of the 52 tsunami victims died on the most severely impacted island of Ghizo, and 21 victims on this island were children (Alertnet, 2007; Reliefweb, 2007b). The government of the Solomon Islands estimated that 30,000 people were affected by the earthquake and tsunami. After the tsunami, many villages lacked suitable housing. Homes were swept away because of the primitive construction techniques traditionally employed on the islands. Most houses have roofs thatched with Sago palm leaves and supported by wooden poles. Many people remain in makeshift hilltop camps, too frightened to return to coastal villages. Mental health issues among the affected populace are of greater concern than is rebuilding, according to a team from the Asian Development Bank, which is working with the government on an emergency assistance project (Disasternews, 2007). The humanitarian disaster attending the earthquake and tsunami led to a convention of many government agencies to determine what lessons were learned that would aid recovery in case of a future disaster (Reliefweb, 2007c).

The 2007 Solomon Islands seism does not appear to have been a "tsunami earthquake," defined as one that produces a tsunami of far greater intensity than would be expected from the considering the earthquake's magnitude alone (Kanamori, 1972; Kanamori and Kikuchi, 1993; Polet and Kanamori, 2000). The teleseismically determined location for the epicenter of the 2007 earthquake is close to the axis of the San Cristobal trench, and a near-trench epicenter characterizes tsunami earthquakes.

However, observations concerning the 2007 earthquake do not accord with the other characteristics of tsunami earthquakes listed in Polet and Kanamori (2000). Perhaps most significant is the observed rupture velocity of 1.95 km/s (Yagi, 2007), which is higher than the low (as low as 1 km/s) rupture velocity typical of tsunami earthquakes (e.g., Ihmlé, 1996; López and Okal, 2006).

A more likely cause for the near-trench epicenter is the warm slab, including an active spreading center, that is being subducted. A warm slab is thought to shift the seismogenic zone up dip along the plate interface and to widen this zone, relative to the cold-slab case (Kirby, 2000; Peacock and Hyndman, 1999; Peacock et al., 1999).

An exceptional tsunami could be caused by an earthquake rupturing inside a sedimentary wedge made up of weak material, which conceptually could lead to enhanced seafloor motion (Fukao, 1979; Okal, 1988). However, MCS data from the Solomon Island arc (Figure 3b) indicate that at least in the northwest part of the rupture area of the 2007 earthquake, the frontal prism is narrow, measured horizontally and perpendicular to the trench, and thin.

Although the 2007 tsunami had dire consequences for the Solomon Islands, the transoceanic tsunami generated by this earthquake had only low amplitude (NGDC, 2007; NOAA, 2007). For example, along the northeast coast of Australia, about 1600 km away from the epicenter, the wave amplitude was about 0.1 m.

To create a preliminary numerical simulation of the April 2007 tsunami, we started with the fault mechanism determined by the Global CMT Project (CMT 2007). The length of the fault that ruptured

was determined from the distribution of aftershocks and from seismic inversions (Ji, 2007; Yagi, 2007).The tsunami-source and -propagation model is based on the method in an earlier study (Geist and Parsons, 2005) that investigated tsunamis from the November 2000 New Ireland earthquake sequence. Animations showing the propagation of the 2007 Solomon Islands tsunami are available on the internet (http://soundwaves.usgs.gov/2007/04/).

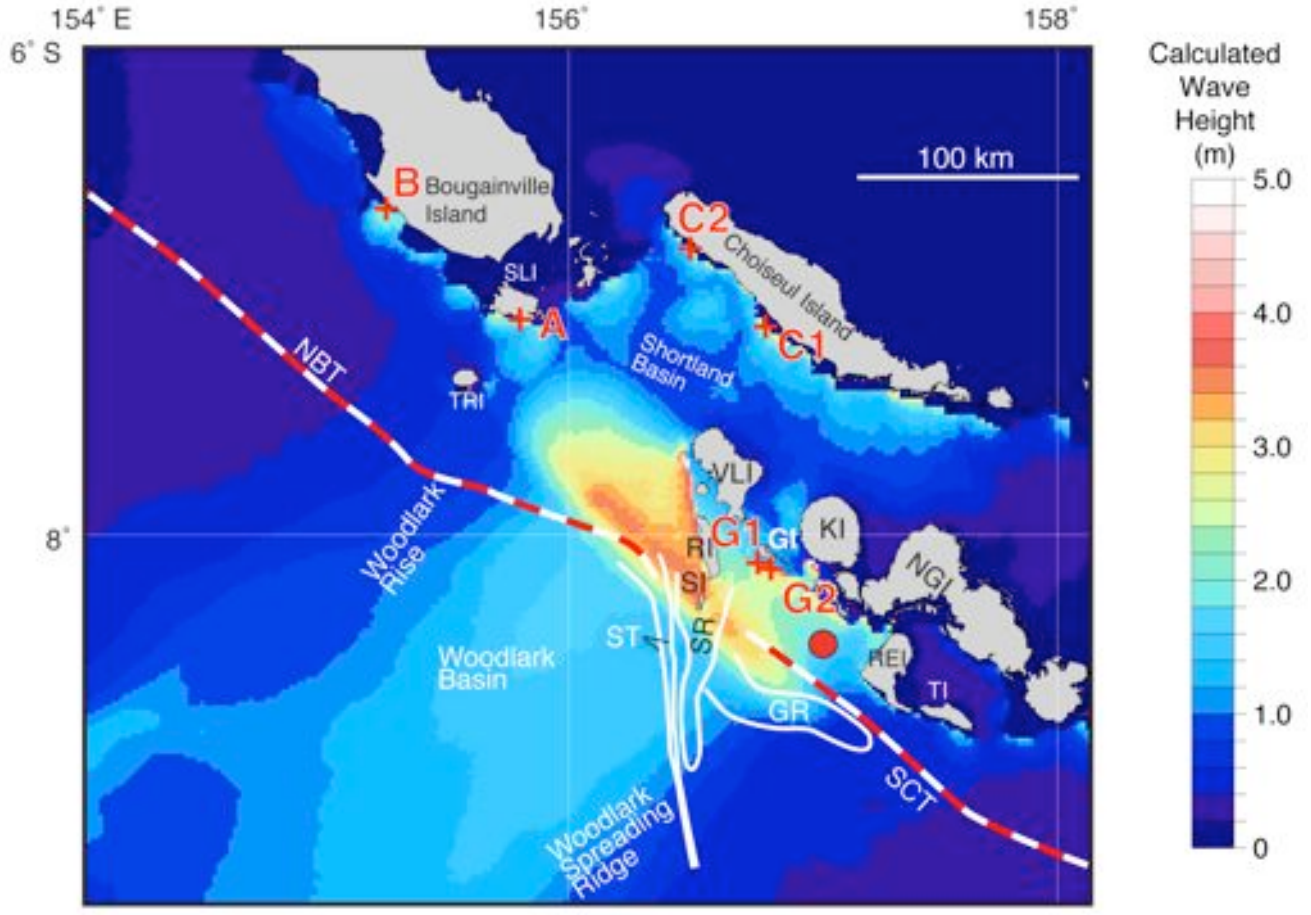

Figure 4. Numerical propagation model of the 2007 tsunami, based on the method in Geist and Parsons (2005). The geographic area depicted here is the same as in Figure 2a. Colors show the distribution of maximum calculated tsunami amplitude that occurred during the first 73 min. of tsunami propagation. Red circle locates the epicenter of the Mw-8.1 earthquake. Dashed red and white lines show trench axes. Red crosses show the locations of the marigrams in Figure 5. Red letters near these crosses refer to specific marigrams. B: Bougainville. C1: Choiseul1. C2: Choiseul2. G1:Ghizo1. G2: Ghizo2. Other abbreviations are as in Figures 2a and 2b.

Coarse-grid propagation modeling is useful for determining the open-ocean beaming pattern for the tsunami. This modeling indicates that the highest offshore amplitudes occurred near the islands of Simbo, Ghizo and Ranungga (Figure 4a), which accords with news reports. It is important to note,

however, that this modeling does not account for propagation near shore, where water is less than 100 m deep. Modeling shallow-water propagation requires high-resolution bathymetry (Titov and Synolakis, 1998). We await field measurements of tsunami inundation to better constrain the tsunami modeling. Also, tsunami modeling can be further refined using the specific slip distribution for this earthquake derived from seismic-waveform analysis (Ji, 2007; Yagi, 2007).

Offshore synthetic marigrams derived from our tsunami modeling indicate that the first tsunami wave arrived at hard-hit Ghizo Island within just 5 min. after the earthquake, and contrary to common expectation, the ocean apparently did not withdraw prior to the tsunami's arrival (Figure 5A). The brief period between the onset of the earthquake and the tsunami's arrival denied people time to realize the imminent danger and react accordingly. In contrast, at islands like Choiseul that are farther away from the trench significant wave heights arrived as much as 20 min. after the earthquake (Figure 5B). Local areas along the coast of Bougainville Island that face the New Britain Trench may have experienced some inundation (Figure 5C).

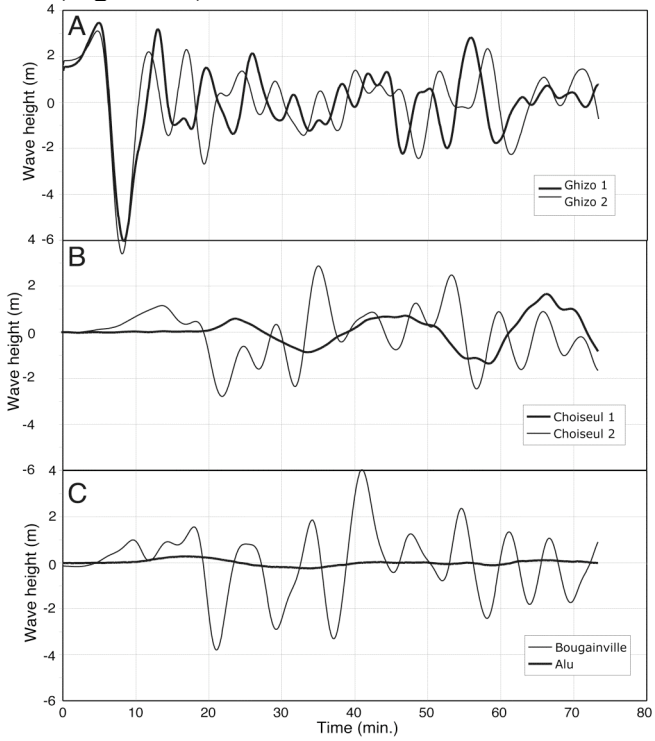

Figure 5A. Synthetic offshore marigrams from the numerical tsunami model showing the calculated wave height for at locations near Ghizo Island, which suffered the worst inundation, for 73 min. after the earthquake. Marigram locations are shown in Figure 4. Water depths at Ghizo1 and Ghizo2 are 142 m and 104 m, respectively.

Figure 5B. Synthetic offshore marigrams near the west coast of Choiseul Island. Marigram locations are shown in Figure 4. Water depths at Choiseul1 and Choiseul2 are 114 m and 114 m, respectively.

Figure 5C. Synthetic offshore marigrams near the west and southwest coasts of Bougainville Island. Marigram locations are shown in Figure 4. Water depths at Bougainville and Alu are 155m and 134 m, respectively.

6. CONCLUSION

The Mw-8.1 earthquake and tsunami that struck the Solomon Islands on April 1, 2007, had substantial long-term impact on local population centers. This earthquake-driven tsunami revealed particular challenges for government agencies in trying to warn local population centers, because only a short time passed between the onset of shaking and arrival of tsunami waves.

The geologic complexity of the plate boundary where the 2007 earthquake struck provides fertile ground for future research. Reprocessing MCS data from other parts of the earthquake's rupture zone will promote better understanding about the origin of this and other tsunamis that originate in subduction zones. Other research topics include the influence of ridge subduction on seismogenesis and the role of splay thrust faults deforming the frontal prism in the generation of tsunamis.

REFERENCES

Alertnet (2007). http://www.alertnet.org/thenews/fromthefield/219478/117984356860.htm

CMT (2007). http://neic.usgs.gov/neis/eq_depot/2007/eq_070401_aqbk/neic_aqbk_hrv.html

Bangs, N. L. B., Shipley, T. H., Gulick, S., Moore, G. F., Kuromoto, S., and Nakamura, Y. (2004). Evolution of the Nankai Trough decollement from the trench into the seismogenic zone: Inferences from three-dimensional seismic reflection imaging: Geology, v. 32, p. 273-276.

Bird, P. (2003). An updated digital model of plate boundaries: G3, v. 4, doi:10.1029/2001GC000252, p. 52 p.

Bruns, T. R., Vedder, J. G., and Cooper, A. K. (1989a). Geology of the Shortland basin region, central Solomons Trough, Solomon Islands--review and new findings, in Vedder, J. G., and Bruns, T. R., eds., Geology and offshore resources of Pacific island arcs--Solomon Islands and Bougainville, Papua New Guinea regions, v. 12: Houston, Texas, Circum-Pacific Council for Energy and Minearal Resources, p. 125-144.

Bruns, T. R., Vedder, J. G., Hart, P. E., and Mann, D. M. (1989b). Multichannel seismic-reflection profiles across the Solomon Islands arc: Guadalcanal-Malaita, Vella Lavella-Choiseul and Bougainville-Buka regions, in Vedder, J. G., and Bruns, T. R., eds., Geology and offshore resources of Pacific island arcs--Solomon Islands and Bougainville, Papua New Guinea regions, v. 12: Houston, Texas, Circum-Pacific Council for Energy and Minearal Resources, p. 323-328.

Cooper, A. K., Bruns, T. R., and Wood, R. A. (1986). Shallow crustal structure of the Solomon Islands intra-arc basins from sonobuoy seismic studies, in Vedder, J. G., Pound, K. S., and Boundy, S. Q., eds., Geology and offshore resources of Pacific island arcs--central and western Solomon Islands, v. 4: Houston, Texas, Circum-Pacific Council for Energy and Minearal Resources, p. 135-156.

Cooper, A. K., Cochrane, G. R., and Bruns, T. R. (1989). Velocity-structure of the upper crust beneath the Solomon Islands-Bougainville island arc, in Vedder, J. G., and Bruns, T. R., eds., Geology and offshore resources of Pacific island arcs--Solomon Islands and Bougainville, Papua New Guinea regions, v. 12: Houston, Texas, Circum-Pacific Council for Energy and Minearal Resources, p. 23-46.

Cooper, A. K., Marlow, M. S., and Bruns, T. R. (1986). Deep structure of the central and southern Solomon Islnads region: Implications for tectonic origin, in Vedder, J. G., Pound, K. S., and Boundy, S. Q., eds., Geology and offshore resources of Pacific island arcs--central and western Solomon Islands, v. 4: Houston, Texas, Circum-Pacific Council for Energy and Minearal Resources, p. 157-175.

Cooper, P. A., and Taylor, B. (1985). Polarity reversal in the Solomon Islands arc: Nature, v. 314, p. 428-430.

Cooper, P. A., and Taylor, B. (1987). A geophysical survey of the Woodlark-Solomons region, in Taylor, B., and Exon, N. F., eds., Marine Geology Geophysics, and Geochemistry of the Woodlark Basin-Solomon Islands, Earth Sci. Ser., v 7: Houston, Texas, Circum-Pac. Counc. Energy Mineral Resour, p. 67-88.

Disasternews, 2007, http://www.disasternews.net/news/article.php?articleid=3213

Fisher, M. A., Collot, J. Y., and Geist, E. L. (1991). Structure of the collision zone between Bougainville guyot and the accretionary wedge of the New Hebrides Island arc, southwest Pacific: Tectonics, v. 10, p. 887-903.

Fukao, Y. (1979). Tsunami earthquake and subduction processes near deep sea trenches: J. Geophys. Res, v. 84, p. 2303-2314.

Geist, E. L., Fisher, M. A., and Scholl, D. W. (1993). Large-scale deformation associated with ridge subduction: Geophys. J. Inter., v. 115, p. 344-366.

Geist, E. L., and Parsons, T. (2005). Triggering of tsunamigenic aftershocks from large strike-slip earthquake: Analysis of the November 2000 New Ireland earthquake sequence: G3, doi:10.1029/2005GC000935, v. 6, p. 1-18.

Goodliffe, A. M., Taylor, B., and Martinez, F. (1999). Data report: Marine geophysical surveys of the Woodlark Basin region, in Taylor, B., Huchon, P., and Klaus, A., eds., Proc. ODP, Init. Repts., 180, 1-134 [CD-ROM]: College Station, TX 77845-9547, U.S.A., Ocean Drilling Program, Texas A&M University.

Ihmlé, P.F. (1996). Frequency-dependent relocation of the 1992 Nicaragua slow earthquake: an empirical Green's function approach. Geophys. J. Internat., v. 127, p. 75-85.

Ji, C. (2007). Rupture process of the 2007 April 1, Magnitude 8.1, Solomon Islands Earthquake: http://earthquake.usgs.gov/eqcenter/eqinthenews/2007/us2007aqbk/finite_fault.php.

Johnson, R. W., Jaques, A. L., Langmuir, C. H., Perfit, M. R., Staudigel, H., Dunkley, P. N., Chappell, B. W., Taylor, S. R., and Baekisapa, M. (1987). Ridge subduction and forearc volcanism: petrology and geochemistry of rocks dredged from the western Solomon island arc and Woodlark Basin (no copy), in Taylor, B., and Exon, N. F., eds., Marine Geology Geophysics, and Geochemistry of the Woodlark Basin-Solomon Islands, Earth Sci. Ser., v 7: Houston, Texas, Circum-Pac. Counc. Energy Mineral Resour, p. 155-226.

Kagan, Y. Y., and Jackson, D. D. (1999). Worldwide doublets of large shallow earthquakes: J. Geophys. Res, v. 89, p. 1147-1155.

Kanamori, H. (1972). Mechanism of tsunami earthquakes: Physics Earth Planetary Interiors, v. 6, p. 346-359.

Kanamori, H. and Kikuchi, M. (1993). The 1992 Nicaragua earthquake: a slow earthquake associated with subducted sediments. Nature, 361: 714-716.

Karig, D. E., and Mammerickx, J. (1972). Tectonic framework of the New Hebrides Island arc: Marine Geology, v. 12, p. 187-205.

Kimura, G., Kitamura, Y., Hashimoto, Y., Yamaguchi, A., Shibata, T., Ujie, K., and Okamoto, S. (2007). Transition of accretionary wedge structures around the up-dip limit of the seismogenic subduction zone: Earth and Planetary Science Letters, v. 255, p. 471-484.

Kirby, S. H. (2000). Taking the temperature of slabs: Nature, v. 403, p. 31-34.

Kondo, H., Kimura, G., Masago, H., Ohmori-Ikehara, K., Kitamura, Y., Ikesawa, E., Sakaguchi, A., Yamaguchi, A., and Okamoto, S. (2005). Deformation and fluid flow of a major out-of-sequence thrust located at seismogenic depth in an accretionary complex: Nobeoka thrust in the Shimanto belt, Kyushu, Japan: Tectonics, v. 24, doi 10.1029/2004TC001655, 16 p.

Kroenke, L. W. (1972). Geology of the Ontong Java Plateau: Hawaii Institute of Geophysics report HIG-72-5, 119 p.

Lay, T., and Kanamori, H. (1980). Earthquake doublets in the Solomon Islands: Physics Earth Planetary Interiors, v. 21, p. 283-304.

López, A.M. and Okal, E.A. (2006). A seismological reassessment of the source of the 1946 Aleutian "tsunami" earthquake. Geophysical Journal International, 165: 835-849.

Mann, P., Taylor, F. W., Lagoe, M. B., Quarles, A., and Burr, G. (1998). Accelerating late Quaternary uplift of the New Georgia Island group (Solomon Island arc) in response to subduction of the recently active Woodlark spreading center and Coleman seamount: Tectonophysics, v. 295, p. 259-306.

Mann, P., and Taira, A. (2004). Global tectonic significance of the Solomon Islands and Ontong Java Plateau convergent zone: Tectonophysics, v. 389, p. 191-220.

Martinez, F., Taylor, B., and Goodliffe, A. M. (1999). Contrasting styles of seafloor spreading in the Woodlark Basin; indications of rift-induced secondary mantle convection: J. Geophys. Res., v. 104, p. 12,909-12,926.

NGDC (2007).
http://www.ngdc.noaa.gov/nndc/struts/results?EQ_0=3037&t=101650&s=9&d=100,91,95,93&nd=display

NOAA (2007). http://www.prh.noaa.gov/ptwc/messages/pacific/2007/pacific.2007.04.02.040500_obs.txt

Okal, E. A. (1988). Seismic parameters controlling far-field tsunami amplitudes: a review: Natural Hazards, v. 1, p. 67-96.

Park, J. O., Tsuru, T., Kodaira, S., Nakanishi, A., Mirua, S., Kaneda, Y., and Kono, Y. (2000). Out-of-sequence thrust faults developed in the coseismic slip zone of the 1946 Nankai earthquake (Mw=8.2) off Shikoku, southwest Japan: Geophysical Research Letters, v. 27, p. 1033-1036.

Park, J. O., Tsuru, T., Kodaira, S., Cummins, P. R., and Kaneda, Y. (2002). Splay fault branching along the Nankai subduction zone: Science, v. 297, p. 1157-1160.

Peacock, S., and Hyndman, R. D. (1999). Hydrous minerals in the mantle wedge and the maximum depth of subduction thrust earthquakes: Geophys. Res. Lett., v. 26, p. 2517-2520.

Peacock, S., Wang, K., and McMahon, A. M. (1999). Seismic consequences of warm versus cool subduction metamorphism: Science, v. 286, p. 937-939.

Phinney, E. J., Mann, W. P., Coffin, M. P., and Shipley, T. H. (1999). Sequence stratigraphy, structure, and tectonic history of the southwestern Ontong Java Plateau adjacent to the North Solomon trench and Solomon Islands arc: J. Geophys. Res, v. 104, p. 20,449-20,466.

Polet, J., and Kanamori, H. (2000). Shallow subduction zone earthquakes and their tsunamigenic potential: Geophys. J. Inter., v. 142, p. 684-702.

Radio New Zealand (2007).
http://www.radionz.co.nz/news/latest/200706041508/6000_homes_destroyed_in_solomons_tsunami

Reliefweb (2007a). http://www.reliefweb.int/rw/RWB.NSF/db900SID/TBRL73EMT6?OpenDocument

Reliefweb (2007b). http://www.reliefweb.int/rw/RWB.NSF/db900SID/EKOI73G7KZ?OpenDocument

Reliefweb (2007c). http://www.reliefweb.int/rw/RWB.NSF/db900SID/LSGZ74CBTA?OpenDocument

Schwartz, S. Y., Lay, T., and Ruff, L. J. (1989). Source process of the great 1971 Solomon Islands doublet: Physics Earth Planetary Interiors, v. 56, p. 294-310.

Schwartz, S. Y. (1999). Noncharacteristic behavior and complex recurrence of large subduction zone earthquakes: J. Geophys. Res, v. 104, p. 23, 111-23,125.

Shinohara, M., Suyehiro, K., and Murayama, T. (2003). Microearthquake seismicity in relation to double convergence around the Solomon Islands arc by ocean-bottom seismometer observation: Geophys. J. Internat., v. 153, p. 691-698.

Taylor, B. (1999). Background and regional setting, in Taylor, B., Huchon, P., Klaus, A., and al., e., eds., Proc. ODP, Init. Repts., 180, 1-134 [CD-ROM]. Available from: Ocean Drilling Program, : College Station, TX 77845-9547, U.S.A., Texas A&M University.

Taylor, B., and Exon, N. F. (1987). An investigation of ridge subduction in the Woodlark-Solomons region: introduction and overview, in Taylor, B., and Exon, N. F., eds., Marine Geology Geophysics, and Geochemistry of the Woodlark Basin-Solomon Islands, Earth Sci. Ser., v 7: Houston, Texas, Circum-Pac. Counc. Energy Mineral Resources, p. 1-24.

Taylor, B., Goodlife, A. M., and Martinez, F. (1999). How continents break up: Insights from Papua New Guinea: J. Geophys. Res, v. 104, p. 7497-7512.

Taylor, F. W., Mann, P., Bevis, M. G., Edwards, R. L., Cheng, H., Cutler, K. B., Gray, S. C., Burr, G. S., Beck, J. W., Phillips, D. A., Cabioch, G., and Recy, J. (2005). Rapid forearc uplift and subsidence caused by impinging bathymetric features: Examples from the New Hebrides and Solomon arcs: Tectonics, v. 24, doi:10.1029/2004TC001650, p. 23 p.

Titov, V.V. and Synolakis, C.E. (1998). Numerical modeling of tidal wave runup: J. Waterway, Port, Coastal, and Ocean Engineering, 124: 157-171.

Tregoning, P., Lambeck, K., Stolz, A., Morgan, P., McClusky, S. C., van der Beek, P., McQueen, H., Jackson, R. J., Little, R. P., Laing, A., and Murphy, B. (1998). Estimation of current plate motions in Papua New Guinea from Global Positioning System observations: J. Geophys. Res, v. 103, p. 12,181-12,203.

Unosat (2007). http://unosat.web.cern.ch/unosat/asp/prod_free.asp?id=81

Wang, K., and Hu, Y. (2006). Accretionary prisms in subduction earthquake cycles: the theory of dynamic Coulomb wedge: J. Geophys. Res, v. 111, doi:10.1029/2005JB004094, 16 pp.

Weissel, J. K., Taylor, B., and Karner, G. D. (1982). The opening of the Woodlark basin, subduction of the Woodlark spreading system, and the evolution of northern Melanesia since mid-Pliocene time: Tectonophysics, v. 87, p. 253-277.

Xu, Z., and Schwartz, S. Y. (1993). Large earthquake doublets and fault plane heterogeniety in the northern Solomon Islands subduction zone: PAGEOPH, v. 140, p. 365-391.

Yagi, Y. (2007). http://www.geo.tsukuba.ac.jp/press_HP/yagi/EQ/20070401/

Yoneshima, S., Mochizuki, K., Araki, E., Hino, R., Shinohara, M., and Suyehiro, K. (2005). Subduction of the Woodlark Basin at the New Britain Trench, Solomon Islands region: Tectonophysics, v. 397, p. 225-239.

A SHALLOW WATER MODEL FOR COMPUTING TSUNAMI ALONG THE WEST COAST OF PENINSULAR MALAYSIA AND THAILAND USING BOUNDARY-FITTED CURVILINEAR GRIDS

Md. Fazlul Karim[a], G D Roy[b], Ahmad Izani M Ismail[a], Mohammed Ashaque Meah[a]

mdfazlulk@yahoo.com ; gaurangadebroy@gmail.com; izani@cs.usm.my; mamsust@yahoo.com

[a] *School of Mathematical Sciences*, *Universiti Sains Malaysia*, 11800 *Pulau Pinang*, *Malaysia*
[b] Department of Mathematics, Shahjalal University of Science & Technology, Sylhet, Bangladesh

ABSTRACT

The west coast of Peninsular Malaysia and Thailand is curvilinear in nature and the bending is especially high along the coast of South Thailand. In hydrodynamic models for coastal seas, bays and estuaries, the use of boundary-fitted curvilinear grids not only makes the model grids fit well with the coastline and bathymetry, but also makes the finite difference scheme simple. In this study, a shallow water model is developed using boundary fitted curvilinear mesh. The west coast of Peninsular Malaysia and Thailand and the western open boundary are represented by two curves, which are defined by two functions. The other two boundaries are considered as straight lines along the open sea. Appropriate transformations of independent coordinates are applied so that the curvilinear physical domain transforms to a rectangular domain and the curvilinear grid system transforms to a rectangular system. The depth averaged shallow water equations and the boundary conditions are transformed to the new space domain and these are solved in the rectangular mesh of the transformed space. The model is applied to compute some aspects of the tsunami associated with the 26 December 2004 Indonesian tsunami along the coastal belts of Penang in Malaysia and Phuket in Thailand. The computed results along the coastal belts are in excellent agreement with the observe data available in the USGS website.

Keywords: boundary-fitted curvilinear grid; shallow water model; Indonesian tsunami 2004

Mathematics Subject Classification: 86A05, 86A17

1. INTRODUCTION

The west coasts of Peninsular Malaysia and southern Thailand face an active seismic tsunami source zone (close to Sumatra Island) along the fault line between the Burma and Indian Plates (Fig. 1). Hence, this coastal belt is vulnerable to the effects of seismic sea waves, or tsunamis generated along this fault line. These events are frequent and often cause little or no damage. However, a great earthquake may generate a large tsunami that may cause extensive loss of life and property damage

Figure 1: Model domain including west coast of Thailand, Peninsular Malaysia and source zone west of north Sumatra (Source: Roy et al. 2006)

along these coastal belts. This was demonstrated on 26 December 2004 when a magnitude 9.3 earthquake, which occurred off the west coast of northern Sumatra, Indonesia, generated a most damaging tsunami. Penang Island in Malaysia and Phuket in Thailand were lashed by high tsunami surges and many lives were lost due to the Indonesian tsunami of 2004.

Numerical computation has become a powerful and popular tool to study tsunamis. A number of papers have been published on modeling the Indonesian tsunami of 2004 for the west coast of Southern Thailand and Peninsular Malaysia after the event 26 December 2004 (see, Roy and Ismail. 2005; Roy et at. 2006; Karim et al. 2006). The analysis area is a rectangular region approximately between 2° N to 14° N and 91° E to 101.5° E for all of these studies. The model area includes the source region of the Indonesian tsunami of 2004. These models are based on depth-averaged shallow water equations and were discretized by the finite-difference scheme in Cartesian coordinate system with the shoreline represented by stair-steps. In a stair step model the coastal boundaries are approximated along the nearest finite difference gridlines of the numerical scheme and so the accuracy of a stair step model depends on the grid size. Since in the stair step models of Roy and Ismail.(2005); Roy et at. (2006) and Karim et al. (2006) very fine resolution were not considered, the representation of the coastal boundaries in those models were not very accurate.

The west coasts of Malaysia and Thailand are curvilinear in nature and the bending is high along the coasts of these countries. Moreover, there are some offshore islands including Penang in Peninsular Malaysia and Phuket in Thailand. For model flows in a rectangular domain, it is natural to use Cartesian grids. Most hydrodynamic models of reservoirs, tidal harbors and estuaries rely on finite difference solution of the depth-averaged equations expressed in a Cartesian coordinate frame (Abbot et al., 1973; Falconer, 1980; Kuipers and Vreugdenhil 1973). In practice, a rectangular mesh with fixed grid spacing is placed over the domain of interest, usually resulting in non-alignment of the physical boundaries with the edges of the computational flow domain. This lack of alignment may give rise to major inaccuracies in the solution. For cylindrical or spherical domains, it is natural to use cylindrical or spherical grids. Hence in the presence of a curvilinear coastline, it is natural to use ‘boundary-fitted’ grids, or generalized curvilinear grids to represent the model boundaries accurately.

Boundary-fitted curvilinear grid systems provide an approach, which combines the best aspects of finite-difference discretisation with grid flexibility. The boundary fitted grid technique makes the equations and boundary conditions simple and better represents the complex geometry with a relatively less number of grid points. Thus, it significantly improves the finite difference schemes. However one difficulty in boundary fitted grid system is that the gridline of the numerical scheme are curvilinear and non-orthogonal. In order to apply a regular finite difference scheme the grid system must be rectangular. In a boundary-fitted model, the curvilinear boundaries are transformed into straight ones using appropriate transformations, so that in the transformed space regular finite difference techniques can be used. Boundary-fitted grid techniques for coastal dynamics have been developed for many regions. Johns et al (1981) used partially boundary-fitted curvilinear grids in their transformed coordinate model for the east coast of India to simulate the surge generated by the Andra Cyclone of 1977. Johns et al. (1981) used a transformation to transform the irregular physical domain

into a rectangular Science of domain. Dube et al. (1985) represented the shoreline of Bangladesh by a curvilinear boundary and used the boundary-fitted curvilinear grids and a transformation, similar to Johns et al. (1981). Roy (1999) developed a mathematical technique to incorporate island of special shapes, each of whose boundaries were approximated along the boundary-fitted grid lines. Following Johns et al.(1981), the transformation of a spatial coordinate was applied so that the physical domain transformed to a rectangular one and the shape of each island also become rectangular in the transformed domain. Johnson (1982) employed the elliptic grid generation technique to study the 2-D vertical-averaged riverine circulation where non-orthogonal boundary-fitted curvilinear grids for the physical domain were generated. Spaulding (1984) built a vertically averaged circulation model using boundary-fitted co-ordinates to simulate the M2 tide in the North Sea. Androsov et al. (1997) made a simulation of tide with a 2-D model in boundary fitted curvilinear mesh.

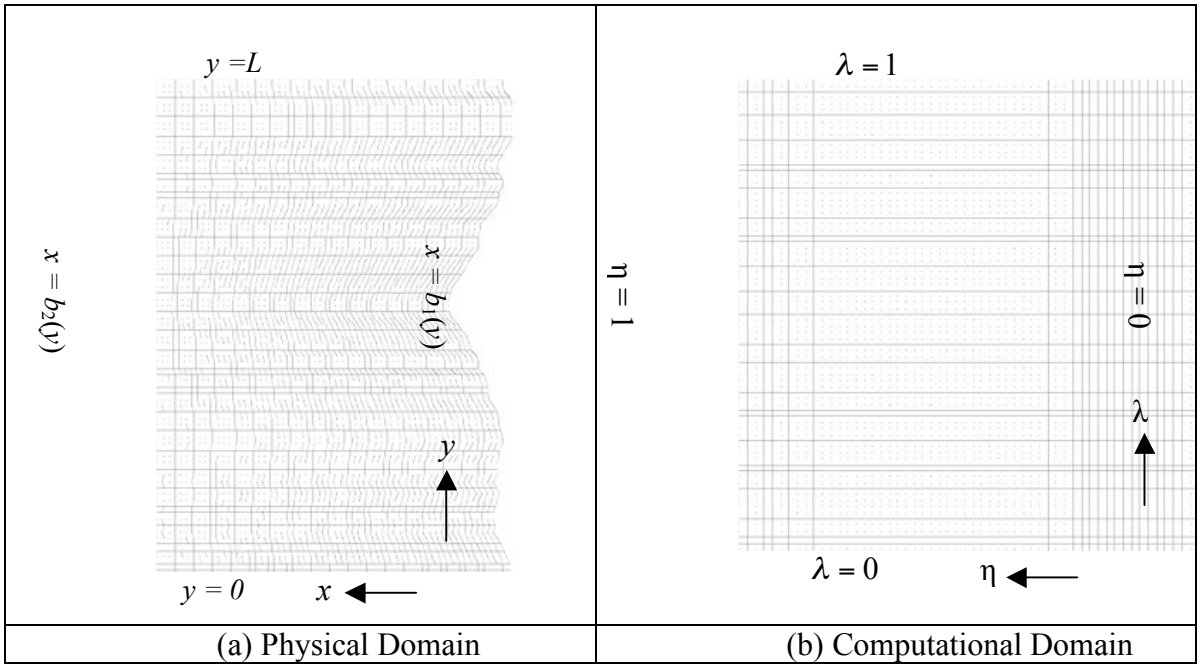

Figure 2: Boundaries and grid system; (a) curvilinear boundaries and the curvilinear grid system, (b) rectangular boundaries and the rectangular grid system

In this paper, a shallow water model is developed using a boundary fitted curvilinear grid system to compute some aspects of the tsunami associated with the Indonesian tsunami of 2004 along the coastal belts of Penang and Phuket. The west coasts of Malaysia and Thailand (curvilinear in nature) and the western open sea boundary were represented by two functions. On the other hand, the north and south open sea boundaries were considered as straight lines. In order to generate a set of non-orthogonal curvilinear grid lines in the model domain and the boundary lines we define two generalized functions. The four boundaries of each island are also represented approximately by these two generalized functions. Two transformations are used so that the physical domain becomes rectangular and the whereabouts of the boundaries of each island are identifiable in the transformed domain. Details of incorporating coastal boundaries and islands are described in section 2.4 and 2.5.

The depth averaged shallow water equations are transformed to the new space domain. These transformed shallow water equations are solved in a rectangular mesh of the transformed grid system in the transformed space using a regular finite difference scheme.

2. GOVERING EQUATIONS AND BOUNDARY CONDITIONS

2.1 *The Original Shallow Water Equations and Boundary Conditions*

The following set of shallow water equations have often been used for modeling tsunami:

$$\frac{\partial \zeta}{\partial t} + \frac{\partial}{\partial x}\left[(\zeta + h)u\right] + \frac{\partial}{\partial y}\left[(\zeta + h)v\right] = 0 \tag{1}$$

$$\frac{\partial u}{\partial t} + u\frac{\partial u}{\partial x} + v\frac{\partial u}{\partial y} - f v = -g\frac{\partial \zeta}{\partial x} - \frac{C_f u\left(u^2 + v^2\right)^{1/2}}{(\zeta + h)} \tag{2}$$

$$\frac{\partial v}{\partial t} + u\frac{\partial v}{\partial x} + v\frac{\partial v}{\partial y} + f u = -g\frac{\partial \zeta}{\partial y} - \frac{C_f v\left(u^2 + v^2\right)^{1/2}}{(\zeta + h)} \tag{3}$$

Here u and v are the x and y components of velocity of sea water respectively, g is gravity, f is Coriolis parameter, ζ is the displacement of the free surface from the equilibrium state, C_f is the bottom friction coefficient, h is ocean depth from the mean sea level.

For numerical treatment it is convenient to express the equations (2) and (3) in flux form by using the equation (1). Equations (1) – (3) may be expressed as

$$\frac{\partial \zeta}{\partial t} + \frac{\partial \tilde{u}}{\partial x} + \frac{\partial \tilde{v}}{\partial y} = 0 \tag{4}$$

$$\frac{\partial \tilde{u}}{\partial t} + \frac{\partial (u\tilde{u})}{\partial x} + \frac{\partial (v\tilde{u})}{\partial y} - f\tilde{v} = -g(\zeta + h)\frac{\partial \zeta}{\partial x} - \frac{C_f \tilde{u}\left(u^2 + v^2\right)^{1/2}}{\zeta + h} \tag{5}$$

$$\frac{\partial \tilde{v}}{\partial t} + \frac{\partial (u\tilde{v})}{\partial x} + \frac{\partial (v\tilde{v})}{\partial y} + f\tilde{u} = -g(\zeta + h)\frac{\partial \zeta}{\partial y} - \frac{C_f \tilde{v}\left(u^2 + v^2\right)^{1/2}}{\zeta + h} \tag{6}$$

where, $(\tilde{u}, \tilde{v}) = (\zeta + h)(u, v)$

2.2 *Boundary Conditions*

For closed (coast) boundaries, the boundary condition is that the normal component of the vertically integrated velocity vanishes and this may be expressed as

$$u\cos\alpha + v\sin\alpha = 0 \qquad \text{for all } t \geq 0 \tag{7}$$

where α denotes the inclination of the outward directed normal to the *x*-axis. It follows that the velocity component *u is* 0 along *y*-directed boundaries and *v is* 0 along *x*-directed boundaries. At the open-sea boundary, the normal component of the velocity cannot vanish and so radiation type of boundary condition is generally used. Following Heaps (1973), the radiation type of boundary condition is

$$u\cos\alpha + v\sin\alpha = -(g/h)^{1/2}\zeta \qquad \text{for all } t \geq 0 \tag{8}$$

Application of a radiation type of boundary condition at the open-sea boundary of a model allows the propagation of energy only outwards from the interior in the form of simple progressive waves.

For $x = b_1(y)$ condition (7) may be simplified as $u + v\tan\alpha = 0$, which implies that $u - v\tan(180-\alpha) = 0$. This can be written as $u - v\dfrac{dx}{dy} = 0$, i.e. $u - v\dfrac{db_1}{dy} = 0$.

Therefore, following Johns et al. (1981), the radiation type of boundary conditions are given by

$$u - v\frac{db_1}{dy} = 0 \qquad \text{at } x = b_1(y) \tag{9}$$

$$u - v\frac{db_2}{dy} = (g/h)^{1/2}\zeta \qquad \text{at } x = b_2(y) \tag{10}$$

$$v + (g/h)^{1/2}\zeta = 0 \qquad \text{at } y = 0 \tag{11}$$

$$v - (g/h)^{1/2}\zeta = 0 \qquad \text{at } y = L \tag{12}$$

2.3 *Boundary-fitted grids*

A system of rectangular Cartesian coordinates is used in which the origin *O*, is within the equilibrium of the sea-surface. *OX* points towards the west, *OY* points towards the north and *OZ* is directed vertically upwards. The displaced position of the sea-surface is given by $z = \zeta(x, y, t)$ and the position of the sea-floor by $z = -h(x, y)$ .The eastern coastal boundary is situated at $x = b_1(y)$ and a western open-sea boundary is at $x = b_2(y)$. The southern and the northern open-sea boundaries are at $y = 0$ and $y = L$ respectively. This configuration is shown in Fig. 2a.

The system of gridlines oriented to $x = b_1(y)$ and $x = b_2(y)$ are given by the generalized function

$$x = \{(k-l)b_1(y) + lb_2(y)\}/k \tag{13}$$

where $k = m$, the number of gridlines in *x*-direction and *l* is an integer with $0 \le l \le k$.

The system of gridlines oriented to $y = 0$ and $y = L$ are given by the generalized function

$$y = \{(q-p)0 + pL\}/q \tag{14}$$

Where $q = n$, the number of gridlines in *y*-direction and *p* is an integer with $0 \le p \le q$.

Note that equation (13) reduces to $x = b_1(y)$ and $x = b_2(y)$ for $l = 0$ and $l = k$ respectively. Similarly equation (14) reduces to $y = 0$ and $y = L$ for $p = 0$ and $p = q$ respectively. Now by proper choice of *l, k* and *p, q* the boundary-fitted curvilinear grids can be generated.

2.4 *Coordinate Transformation*

To facilitate the numerical treatment of an irregular boundary configuration, a coordinate transformation is introduced, similar to that in Johns et al. (1985), which is based upon a new set of independent variables η, λ, y, t where

$$\eta = \frac{x - b_1(y)}{b(y)}, \quad \lambda = \frac{y}{L}, \quad b(y) = b_2(y) - b_1(y) \tag{15}$$

This mapping transforms the analysis area enclosed by $x = b_1(y), x = b_2(y), y = 0$ and $y = L$ into a rectangular domain given by $0 \le \eta \le 1, \quad 0 \le \lambda \le 1$. Also the generalized function (13) takes the form

$b\eta + b_1 = \{(k-l)b_1(y) + lb_2(y)\}/k$

which can be written as

$\eta = \frac{l(b_2 - b_1)}{bk}$. This means

$$\eta = \frac{l}{k} \tag{16}$$

The generalized function (14) takes the form
$\lambda L = \{(q-p)0 + pL\}/q$, which implies

$$\lambda = \frac{p}{q} \tag{17}$$

For $l = 0$, we have the eastern coastal boundary $\eta = 0$ or $x = b_1(y)$ and for $l = k$ we have the western open-sea boundary $\eta = 1$ or $x = b_2(y)$. Similarly, for $p = 0$, we have the southern open sea boundary $\lambda = 0$ or $y = 0$ and for $p = q$ we have the northern open-sea boundary $\lambda = 1$ or $y = L$. Thus by the proper choice of the constants k and q and the parameters l and p, a rectangular grid system can be generated in the transformed domain. Figures 2a and 2b show the physical and transformed domains and their grids.

2.5 ***Representation of Islands***

Every boundary of each island has been broken into several segments and every segment has been aligned either along (13) or along (14) so that the boundaries of every island are aligned along the boundary fitted gridlines. The representation of the island boundaries are done in such a way so that the whereabouts of them have not been lost in the transformed domain. Each of the eastern and western boundaries of an island is given by (13) and each of the southern and northern boundaries of an island is given by (14).

$l = 0$ implies $x = b_1(y)$ or $\eta = 0$ i.e. the coastal boundary and $l = k$ implies $x = b_2(y)$ or $\eta = 1$ i.e. the open boundary. Equation (13) with two different values of l, say, l_1 and l_2 with $l_1 < l_2$ will express the eastern and western boundaries of an island. Similarly equation (14) with two different values of p, say p_1 and p_2 with $p_1 < p_2$, will express the south and north boundaries of the island. Thus the transformed boundaries of an island are expressed as

$$\eta = l_1/k,\ \eta = l_2/k,\ \lambda = p_1/q, \lambda = p_2/q \tag{18}$$

2.6 ***Transformed Shallow Water Equations and Boundary Conditions***

By using the transformations (15), we have

$$\frac{\partial}{\partial x} \equiv \frac{1}{b}\frac{\partial}{\partial \eta} \tag{19}$$

$$\frac{\partial}{\partial y} \equiv -\frac{1}{b}\left(\frac{db_1}{dy} + \eta\frac{db}{dy}\right)\frac{\partial}{\partial \eta} + \frac{1}{L}\frac{\partial}{\partial \lambda} \tag{20}$$

Taking η, λ, y, t as the new independent variables and using the relations (19) and (20), the equations (4) – (6) transform to

$$\frac{\partial (bL\xi)}{\partial t} + \frac{\partial \tilde{U}}{\partial \eta} + \frac{\partial \tilde{V}}{\partial \lambda} = 0 \tag{21}$$

$$\frac{\partial \tilde{u}}{\partial t} + \frac{\partial (U\tilde{u})}{\partial \eta} + \frac{\partial (V\tilde{u})}{\partial \lambda} - f\tilde{v} = -gL(\xi + h)\frac{\partial \xi}{\partial \eta} - \frac{C_f \tilde{u}\left(u^2 + v^2\right)^{1/2}}{\xi + h} \tag{22}$$

$$\frac{\partial \tilde{v}}{\partial t} + \frac{\partial (U\tilde{v})}{\partial \eta} + \frac{\partial (V\tilde{v})}{\partial \lambda} + f\tilde{u} = -g(\xi + h)\left[b\frac{\partial \xi}{\partial \lambda} - L\left(\frac{db_1}{dy} + \eta \frac{db}{dy}\right)\frac{\partial \xi}{\partial \eta}\right] - \frac{C_f \tilde{v}\left(u^2 + v^2\right)^{1/2}}{\xi + h} \tag{23}$$

where, $U = \frac{1}{b}\left[u - \left(\frac{db_1}{dy} + \eta \frac{db}{dy}\right)v\right]$, $V = \frac{v}{L}$, $(\tilde{u}, \tilde{v}, \tilde{U}, \tilde{V}) = bL(\xi + h)(u, v, U, V)$

At $x = b_1(y)$ *i.e.* at $\eta = 0$,

$$U = \frac{1}{b}\left[u - \left(\frac{db_1}{dy} + \eta \frac{db}{dy}\right)v\right] = \frac{1}{b}\left[u - \frac{db_1}{dy}v\right] = 0.$$

At $x = b_2(y)$ *i.e.* at $\eta = 1$,

$U = \frac{1}{b}\left[u - \left(\frac{db_1}{dy} + 1 \cdot \frac{db}{dy}\right)v\right] = \frac{1}{b}\left[u - \frac{db_2}{dy}v\right]$, which can be written as $bU = u - \frac{db_2}{dy}v$.

Therefore the boundary conditions (9) – (12) reduces to

$U = 0$ at $\eta = 0$ (24)

$bU - (g/h)^{1/2}\xi = 0$ at $\eta = 1$ (25)

$VL + (g/h)^{1/2}\xi = 0$ at $\lambda = 0$ (26)

$VL - (g/h)^{1/2}\xi = 0$ at $\lambda = 1$ (27)

At each boundary of an island, the normal component of the velocity vanishes. Thus, the boundary conditions of an island are given by

$U = 0$ at $\eta = l_1 / k$ and $\eta = l_2 / k$ (28)

$V = 0$ at $\lambda = p_1 / q$ and $\lambda = p_2 / q$ (29)

3. Numerical Discretisation

The transformed shallow water equations and boundary conditions were discretised on a staggered (η, λ) grid and solved by a finite difference scheme.

We define the grid points (η_i, λ_j) in the domain by

$$\eta = \eta_i = (i-1)\Delta\eta, \qquad i = 1, 2, 3, \ldots, m \tag{30}$$

$$\lambda_j = (j-1)\Delta\lambda, \qquad j = 1, 2, 3, \ldots, n \tag{31}$$

The sequence of discrete time instants is given by

$$t_k = k\,\Delta t, \qquad k = 1, 2, 3, \ldots \tag{32}$$

The curvilinear grid system is generated through (13) and (14). In the transformed domain the corresponding rectangular grid system is generated through (16) and (17) with appropriate choices of k, q, p and l. The curvilinear boundaries and grids in the physical domain and the corresponding rectangular boundaries and grids in the computational domain are shown in Fig. 2.

The η-axis is directed towards west at an angle 15° (anticlockwise) with the latitude line and the λ-axis is directed towards north inclined at an angle 15° (anticlockwise) with the longitude line through the origin. In this model the analysis area is extended from 2° N to 14° N latitudes (incorporating the west coasts of Malaysia including Penang and Southern Thailand including Phuket) and 91° E to 100.5° E longitudes. The number of grids in η and λ - directions are respectively m = 230 and n = 319. The model area includes the source region of the Indonesian tsunami of 2004. At the ocean boundary, radiation condition, in which the tsunami wave is assumed to go out without changing its shape, is assumed. At the land boundary (coast), total reflection is assumed. The coastal boundary is fixed; that is, no run-up on the land is considered. The time step of computation is determined so as to satisfy the stability condition (Courant condition) and is set to 10 s in this computation. Following Kowalik et al. (2005), the value of the friction coefficient C_f is taken as 0.0033 throughout the model area. The depth data for the model area are collected from the Admiralty bathymetric charts.

4. Initial condition

Tsunami generation is commonly modeled by assuming that the initial sea surface displacement is formed by the permanent vertical displacement of the ocean bottom induced by an earthquake. The generation mechanism of the 26 December 2004 tsunami was mainly due a static seabed deformation caused by an abrupt slip at the India/Burma plate interface. The estimation of the extent of the earthquake rapture as well as the maximum uplift and subsidence of the seabed is given in Kowalik et. al.(2005). From the deformation contour, it is seen that the estimated uplift and subsidence zone is between 92° E to 97°E and 2°N to 10°N with a maximum uplift of 507 cm at the west and maximum subsidence of 474 cm at the east so that the uplift to subsidence is approximately from west to east. We assume that this sea surface displacement is the same as the ocean bottom displacement, due to incompressibility of the ocean. Following Kowalik et. al. (2005) the disturbance in the form of rise and fall of sea surface is assigned as the initial condition in the model with a maximum rise of 5 m to maximum fall of 4.75 m to generate the response along the western open boundary. In all other regions the initial sea surface deviations are taken as zero. Also the initial velocity components in η and λ - directions are taken as zero throughout the model area.

5. Results and Discussions

In this section, numerical results are given for the model described in the previous sections. Wave propagation from the source is computed and the water levels along the coastal belts of Phuket and Penang Islands are estimated. Every computed water level is measured with respect to the mean sea level.

Figure 3 shows the time, in minutes, for attaining +0.1 m sea level rise computed through the model. Considering the 0.1 m sea level rise as the arrival of tsunami, it is seen that after generating the initial tsunami wave at the source region, the disturbance propagates gradually towards the coast. The arrival times of initial tsunami at Phuket and Penang Island are approximately 110 min and 240 min. According to USGS report the tsunami waves reached at Phuket within two hours time after the earthquake [(http://staff.aist.go.jp/kenji.satake/Sumatra-E.html) (Tsunami travel time in hours for the entire Indian Ocean)]. The above USGS website data also confirms the fact that the tsunami waves reached Penang Island four hours after the earthquake. Hence the time of tsunami strike at the coastal regions matches well with the observations. In an earlier study (Roy et al. 2006), it is reported that the tsunami waves reached at Phuket and Penang Islands within 90 min and 230 min respectively. While the agreement of earlier study is quite good, there is a slightly better agreement in timing in the present study using boundary-fitted curvilinear grids.

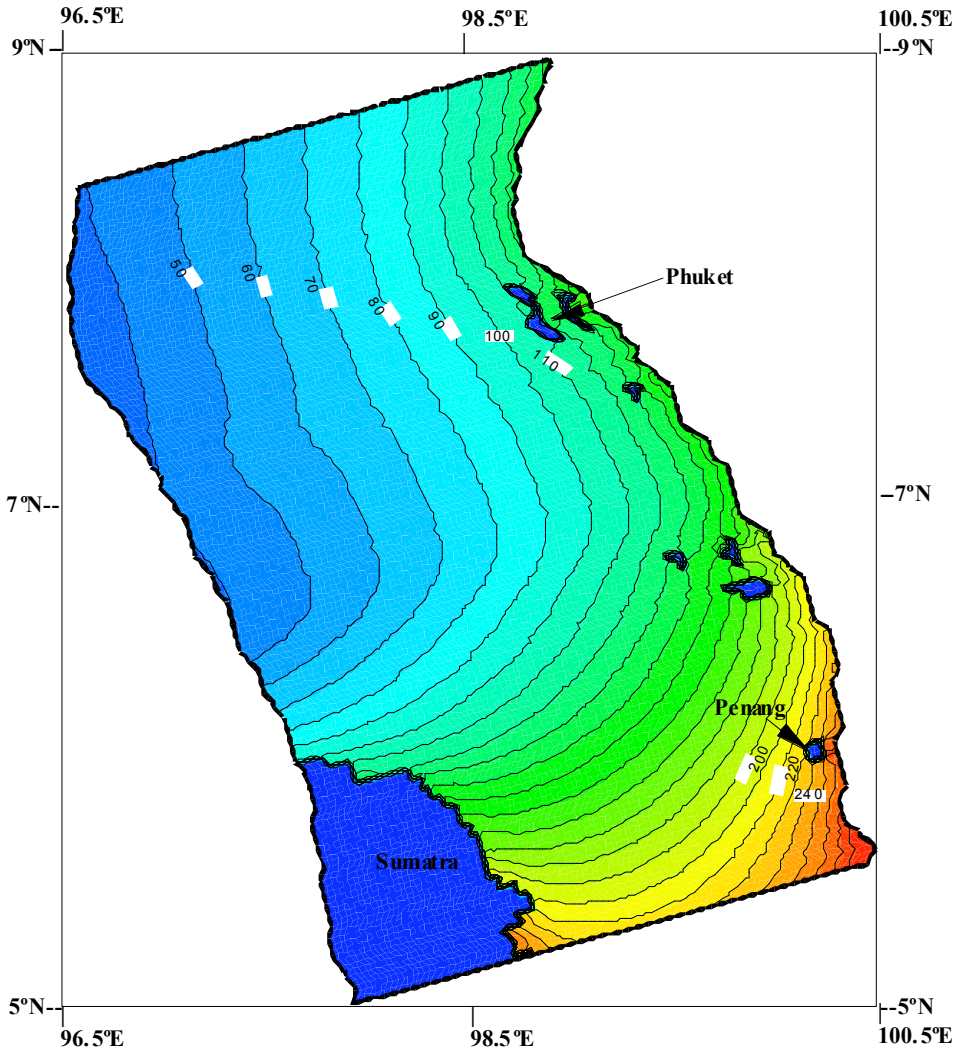

Figure 3: Tsunami propagation time in minutes towards Phuket and Penang Islands

The propagation of the tsunami towards the west coast of Peninsular Thailand and Malaysia can also be seen in Fig. 4, where the sea surface disturbance pattern is shown at four different instants of time. At 60 min after the generation of the initial tsunami wave at the source, the sea surface disturbance is found to be proceeding towards Phuket (Fig. 4a). At 110 min the tsunami has proceeded considerably towards Penang Island after flooding the Phuket region (Fig. 4b). In 180 min the disturbance propagates further towards Penang Island and finally at 240 min the tsunami surge is hitting the north and west coasts of Penang Island (Fig. 4c, d).

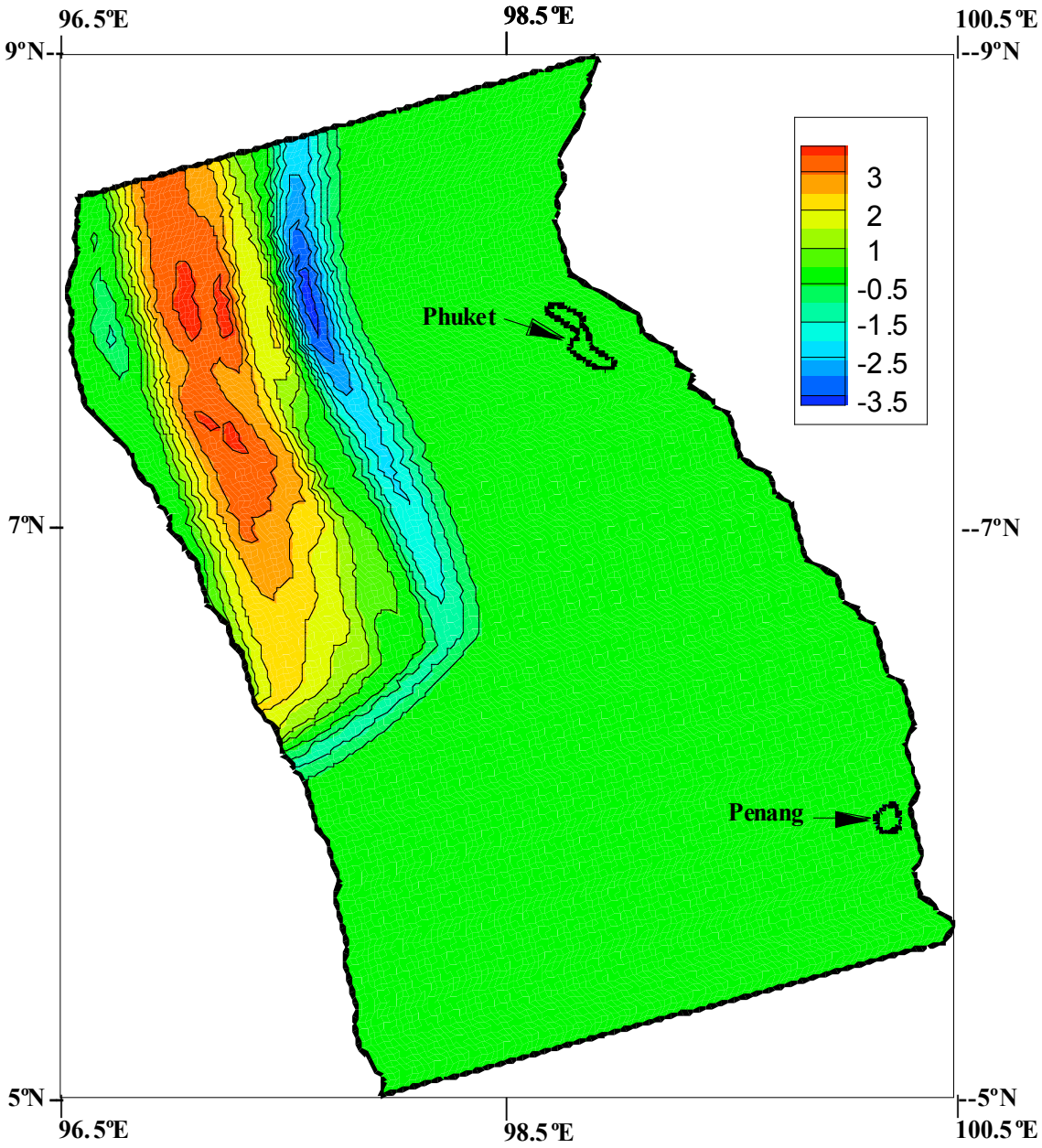

Figure 4a: Computed tsunami disturbance pattern at 60 min

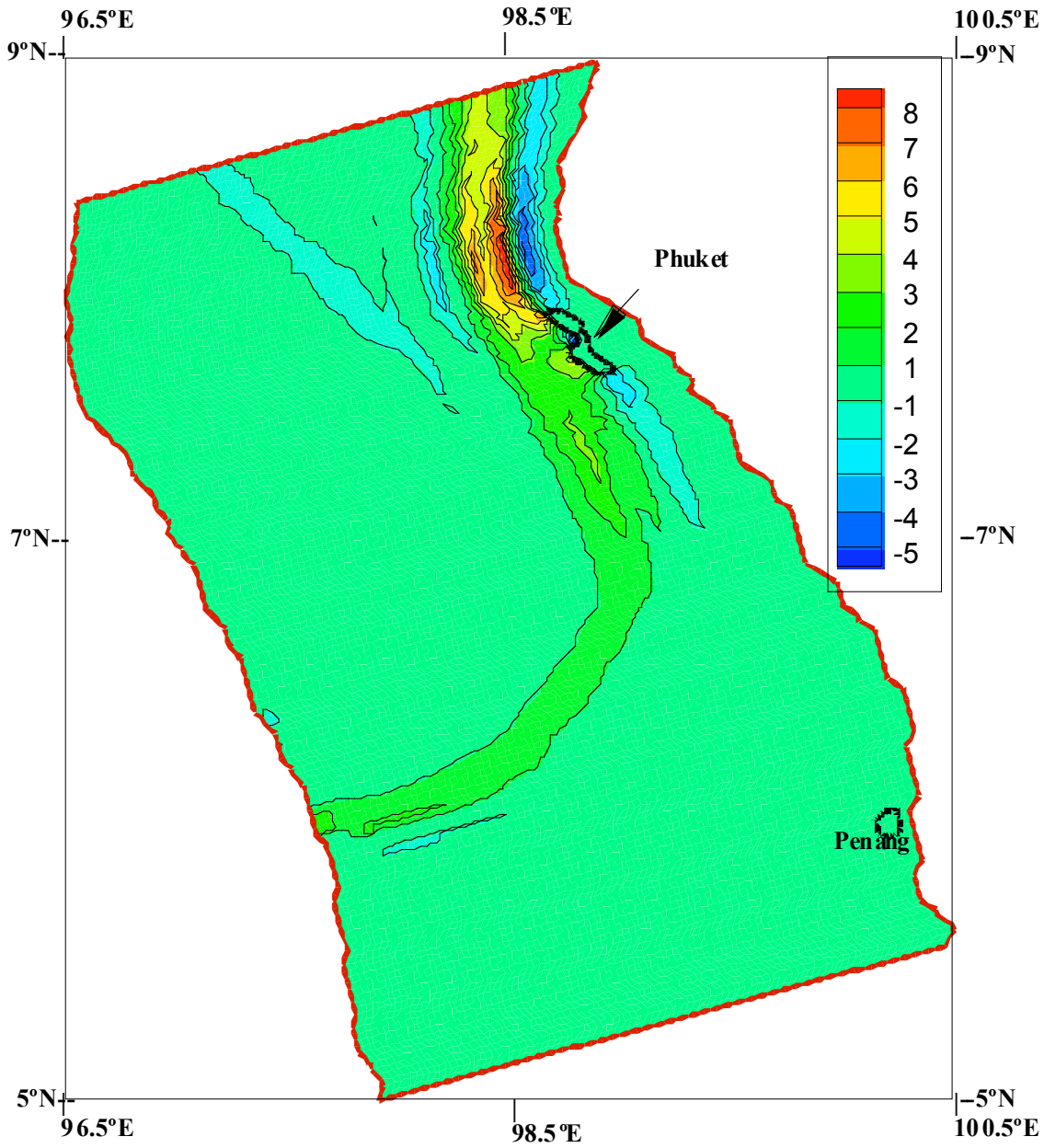

Figure 4b: Computed tsunami disturbance pattern at 110 min

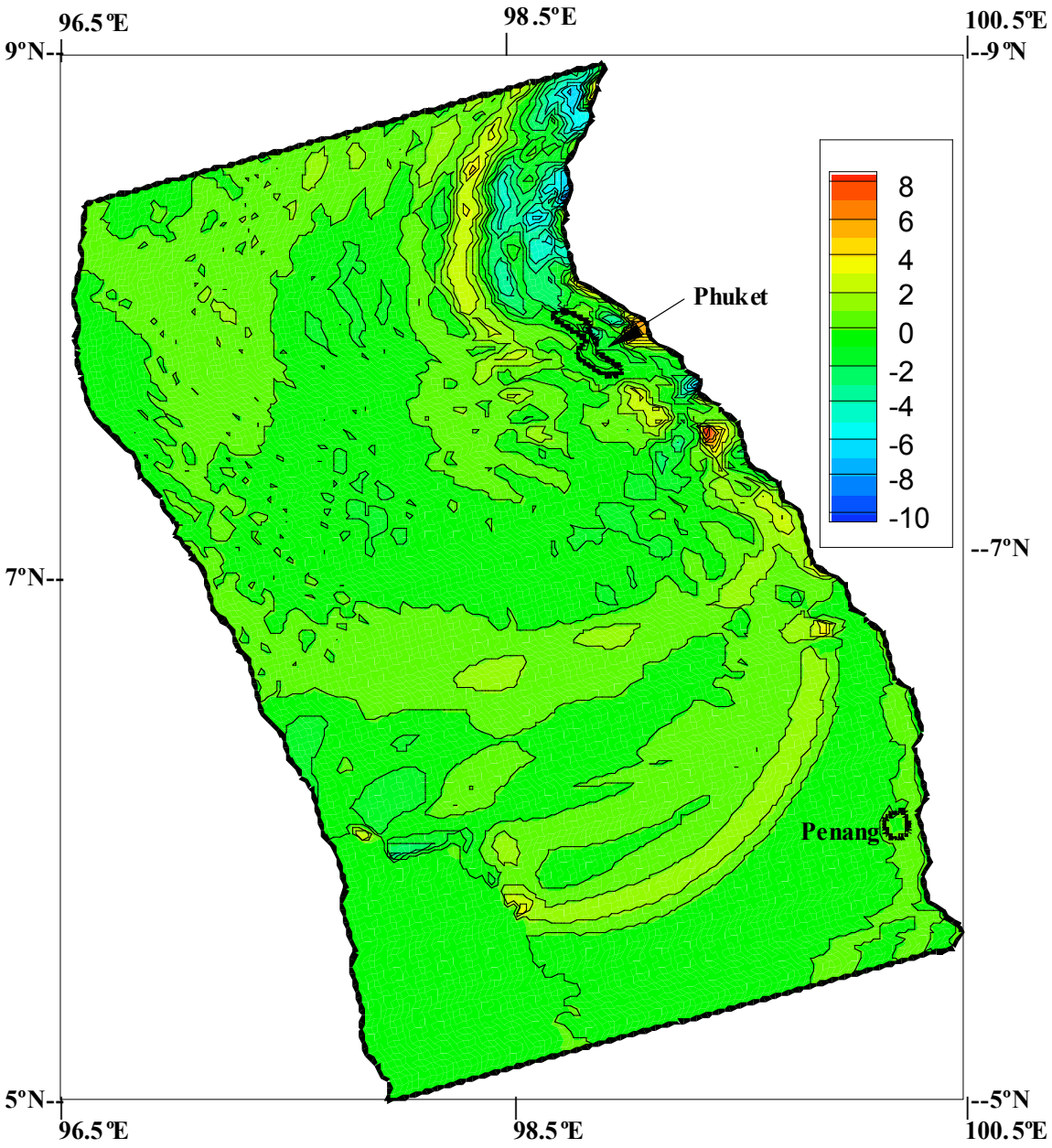

Figure 4c: Computed tsunami disturbance pattern at 180 min.

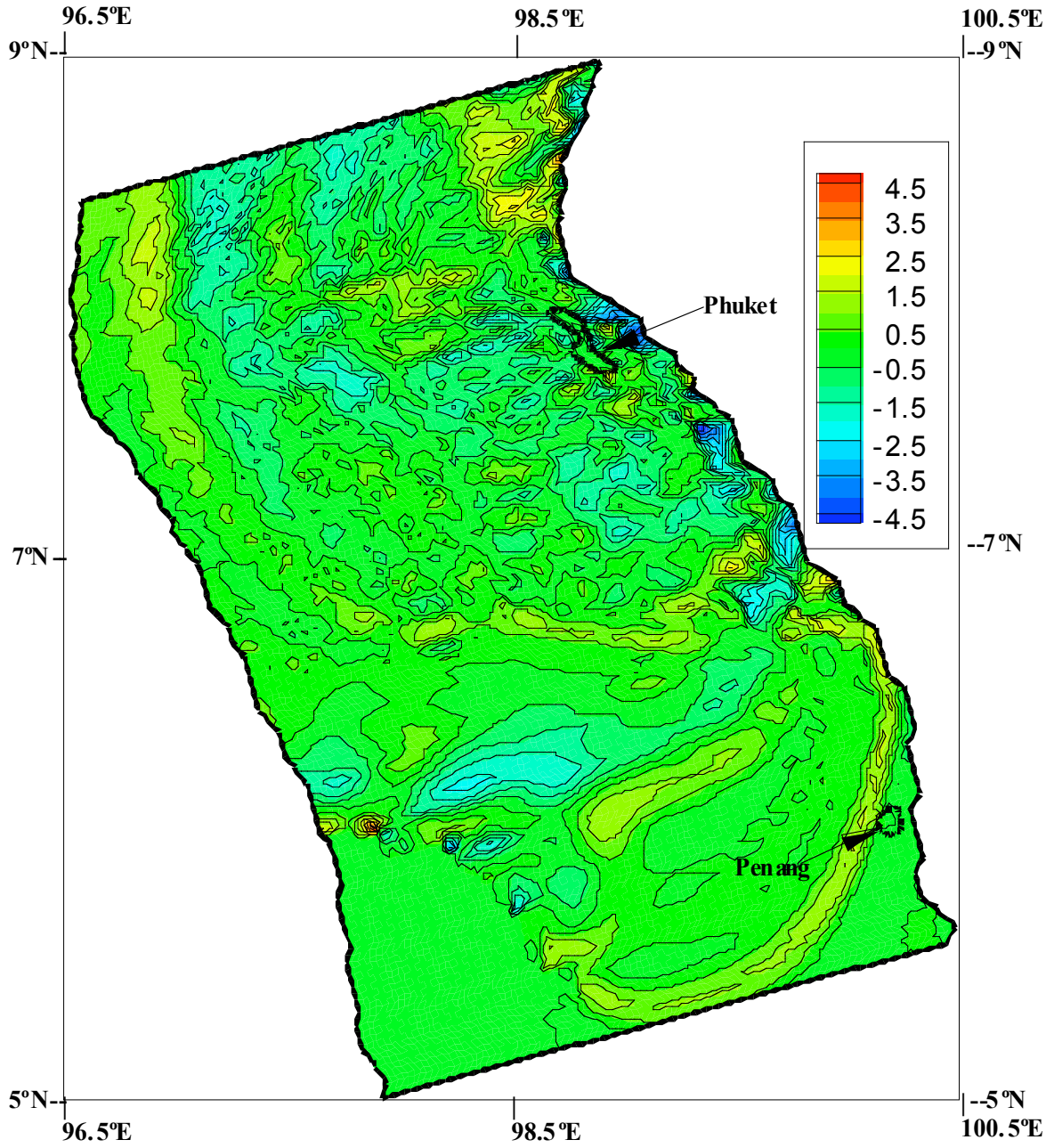

Figure 4d: Computed tsunami disturbance pattern at 240 min.

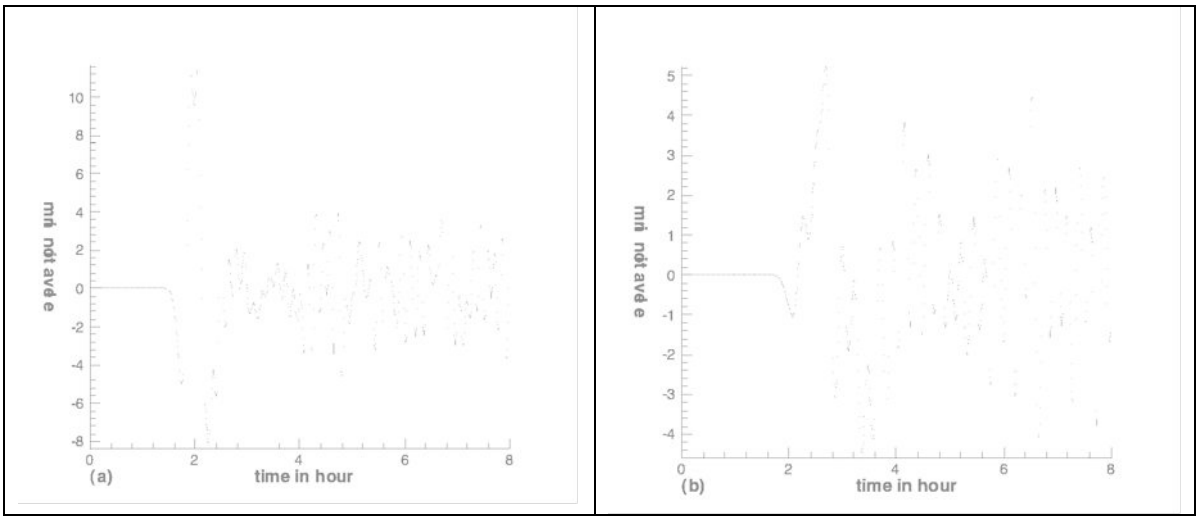

Figure 5: Time series of computed elevations at two coastal locations of Phuket Island: (a) West coast; (b) East coast

The computed water levels at different locations of the coastal belt of Phuket and Penang Island are stored at an interval of 30 seconds. Figure 5 depicts the time series of water levels at two locations of Phuket. At the west coast, the fluctuation begins with recession that reaches up to minimum level of –8.0 m before rising up; then the water level gradually increases to reach a maximum level of 11.6 m. The fluctuation then continues for several hours with low amplitude (Fig. 5a). At the east coast of Phuket also the fluctuation begins with recession reaching a minimum level of – 4.4 m. Then the water increases to a maximum level of 5.2 m before going down again; the oscillation then continues with low amplitude (Fig. 5b). Figure 6 shows the time series of water levels at two locations of Penang Island. At Batu Ferringi (north coast) the fluctuation begins with recession; the minimum and maximum levels attained are respectively – 3.4 m and 2.6 m (Fig. 6a). At the west coast the fluctuation is also oscillatory with minimum and maximum elevations of – 2.2 m and 3.2 m respectively (Fig. 6b).

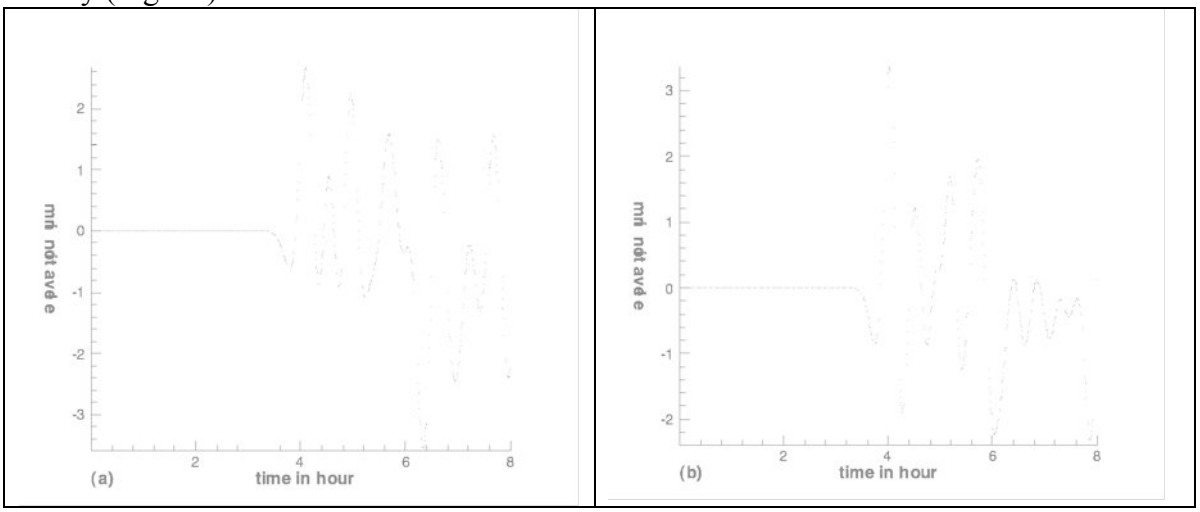

Figure 6: Time series of computed elevations at two coastal locations of Penang Island: (a) North coast; (b) West coast.

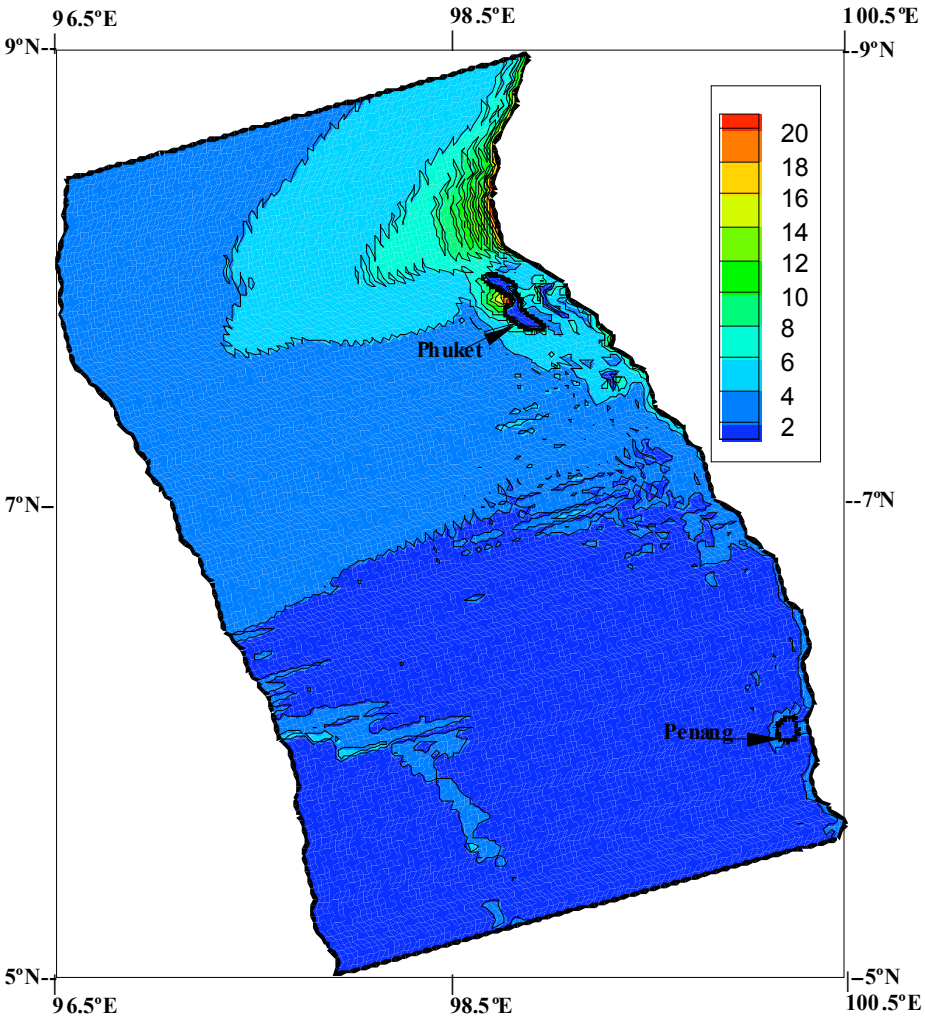

Figure 7: Contour of maximum elevation around Phuket and Penang Islands.

Figure 7 depicts the maximum water level along the west coast of Peninsular Malaysia and Thailand. It is found that the maximum water level gradually decreases in the southern direction. In the Phuket region the maximum water level ranges from 6 m to 12 m from south to north. The maximum coastal surge estimated by this model varies from 18 - 20 m in some locations located approximately 50 km north from the Phuket. We compare the computed maximum surge levels with that available in the website (www.drgeorgepc.com/Tsunami2004/Indonesia.html) and Tsuji et al. (2006). In this website address it is reported that wave height reached 7 to 11 m surrounding Phuket Island. Tsuji et al. (2006) reported that the largest tsunami height reached up to 19.6 m at Ban Thung Dap located at 50 km north from the Phuket. Thus, comparison with USGS website and study of Tsuji et al. (2006) is quite good for the Phuket region. Roy et al. (2006) reported that the computed

maximum water level at Phuket region is from 3.5 m to 7 m. So the coastal surge estimated by the present model shows better agreement with USGS than that of Roy et al. (2006).

The maximum elevation at Penang Island ranges from 2 m to 4 m along the west coast with an increasing trend towards the north. On the east coast, the measures tsunami heights show a decreasing trend towards the north. The coastal surge estimated by this model for Penang region matches reasonably well with the reported information of Roy et al. (2006).

6. Conclusions and recommendations

The results of this study indicate that boundary-fitted shallow water model is a powerful tool for simulating tsunami along a coastal belt, which is curvilinear in nature. As compared with other models, this model can make the grids fit the boundaries and can facilitated the handling of boundary conditions as well as the numerical simulation. Thus, the model has high simulation accuracy, especially in the vicinity of boundaries.

A shortcoming of the curvilinear boundary fitted representation is its inability to represent coastal and islands orographical detail. To incorporate the bending of coasts and the offshore islands with considerable accuracy in the numerical scheme, a very fine mesh numerical scheme is necessary. A nested numerical scheme (inner model with fine resolution) within the original model (outer model with high resolution) can be developed to record the fine orographical detail in the regions of principal interest. This work is ongoing and findings will be reported in our subsequent paper.

Acknowledgements

The authors acknowledge financial support from a short-term grant of University Sains Malaysia.

REFERENCES

Abbott, M.B., Damsgaard, A., Rodenhuis, G.S. 1973: System 21, 'Jupiter' A design system for two-dimensional nearly-horizontal flows, J. of Hydraulic Research, 11(1), 1 -28.

Androsov, A. A., Vol'tzinger, N. E., Liberman, Y. M. 1997: A two-dimensional tidal model of the Barents Sea. Oceanology, 37, 16-22.

Dube, S.K., Sinha, P.C., Roy, G.D. 1985: The Numerical Simulation of Storm Surge along the Bangladesh. Coast. Dyn. Atms. Oceans, 9, 121-133.

Falconer, R.A. 1980, Numerical modeling of tidal circulation in harbours, J. Waterway, Port, Coastal and Ocean Div., Proc. ASCE, 106, WW1, 31 – 48.

Heaps, N. S. 1973. A three dimensional numerical model of the Irish Sea. Geophys. J. Astorn. Soc. 35, 99 - 120.

Johnson, B.H. 1982. Numerical modeling of estuarine hydrodynamics on a boundary-fitted coordinate system in Numerical Grid Generation (Thompson, J., ed.). Elsevier, 419-436.

Johns B. Dube, S.K. Mohanti, U.C., Sinha, P.C. 1981: Numerical Simulation of surge generated by the 1977 Andhra cyclone; Quart. J. Roy. Soc. London 107, 919 – 934.

Karim, M. F., Roy, G. D., Ismail, A. I. M., and Meah, M. A. 2006, A linear Cartesian coordinate shallow water model for tsunami computation along the west coast of Thailand and Malaysia. Int. J. Ecol. & Dev., 4(S06), 1-14.

Kowalik, Z., Knight, W., Logan, T., and Whitmore. P. 2005, Numerical Modeling of the Global Tsunami: Indonesian Tsunami of 26 December 2004, Sc. of Tsunami Hazards, 23(1), 40-56.

Pararas-Carayannis, G. (2005) http://www.drgeorgepc.com/Tsunami 2004/Indonesia.html

Roy, G.D., Izani, A. M. I. 2005, An investigation of 26 December 2004 tsunami waves towards the west coast of Malaysia and Thailand using a Cartesian coordinates shallow water model, Proc. Int. Conf. Math. & Applications, Mahidol University, Thailand, 389 – 410.

Roy, G. D., Karim, M. F., Ismail, A. M.; 2006, Numerical Computation of Some Aspects of 26 December 2004 Tsunami along the West Coast of Thailand and Peninsular Malaysia Using a Cartesian Coordinate Shallow Water Model. Far East J. Appl. Math. 25(1): 57-71.

Roy, G. D., Humayun Kabir, A. B. M., Mandal, M. M., Haque, M. Z. 1999, Polar Coordinate Shallow Water storm surge model for the coast of Bangladesh, Dyn. Atms. Ocean, 29, 397-413.

Spaulding, M.L. (1984). A Vertical Averaged Circulation Model Using Boundary-fitted Coordinates. Journal of Physical Oceanography, 14, 973-982.

Tsuji, Y., Namegaya, Y., Matsumoto, H., Iwasaki, S., Kanbua, W., Sriwichai, M., Meesuk, V. 2006, The 2004 Indian tsunami in Thailand: Surveyed runup heights and tide gauge records, Earth Planets Space, 58, 223-232.

REFRACTION OF TSUNAMI WAVES OF 26 DECEMBER 2004, ALONG SOUTHWEST COAST OF INDIA

K.K.Varma* and A. Sakkeer Hussain
Dept. of Fishery Hydrography, College of Fisheries
Panangad, Kochi – 682506.

ABSTRACT

In this paper the refraction of the tsunami of 26 December 2004, which caused severe damage along the south west coast of India has been studied. Wave refraction diagrams for the possible wave directions indicate convergence around the places like Kolachel, around Kollam and Alappuzha, where greater destructions occurred due to this tsunami and divergence at the places spared by the tsunami. Broad areas vulnerable to tsunamis have been identified. Possible causes for increased destruction in Kolachel at the southern tip of Indian peninsula are discussed. Bottom topography is one of the factors that determine the intensity of the tsunami waves. Bottom steering is caused by the wave refraction. Comparatively gentler sloping topography in a zone north of Kollam at depths beyond 200m and the topographic dome off Kollam appear to have influence on determining the impact of tsunamis.

- For correspondence (E-mail: varmacochin@yahoo.com)

Science of Tsunami Hazards, Vol. 26, No. 1, page 42 (2007)

INTRODUCTION

The great Indian Ocean tsunami was caused by an earthquake of magnitude 9.3 on the Richter scale (Javed *et al.*, 2005) on December 26, 2004 at 06:28 IST (Chadha *et al.*, 2005) off the western coast of northern Sumatra. The epicentre of the earthquake was at about 3.32^{o} N & 95.85^{o} E, at a depth of about 30 km below mean sea level (http://earthquake.usgs.gov/eqcenter/eqinthenews/2004/usslav). The length of the tsunami source region has been estimated by backward ray tracing to be about 600 km (Lay *et al*., 2005). This has been re-estimated by Neetu *et al.,* (2005) to be about 900 km. The tsunami severely hit mainly Srilanka, Indonesia and India, although some other littoral countries of the Indian Ocean were also affected. The death toll is reported to be more than 2,50,000 (Chadha *et al.*, 2005).

The arrival time of tsunami waves at Colombo, Chennai and Cochin were 0352, 0335, 0541 UTC (IST is 5.30 hours ahead of UTC) respectively (Nagarajan *et al.*, 2006). The affected places along southwest coast of India were around Kollam, Alappuzha and Ernakulam districts in Kerala and the Kanyakumari district in Tamil Nadu (see figure 1). Compared to the east coast, the impact was less along the west coast. Although the impact decreased from south to north, it varied from place to place along the coastline. The impact at Ernakulam district was lesser compared to affected areas further south.

Figure 1. Tsunami affected districts along the southwest coast of India.

The main objective of the present study was to generate the wave refraction diagrams for different directions of approach in the December 2004 tsunami along the southwest coast of India. For the tsunami, the processes that occur as waves approach to the shore is the convergence and divergence of energy, due to wave refraction. This causes greater damage and loss of life in some area, while the other area in the neighbourhood may remain unaffected. It is important to know the possible areas of

damage and destruction and wave refraction studies are useful to identify these areas. Varma and Sakkeer (2005), presented preliminary results of refraction of tsunami, limiting to the study area to the Kerala coast. In the present study, the area is extended and the coastline between Kanyakumari and Cochin is considered.

Waves in shallow water and tsunami

Tsunamis are very long waves, with large dimensions in width. For such waves approaching from easterly direction, Srilanka and the peninsular India act as barriers and diffraction brings the waves to the Arabian Sea. On examining the simulations available in the internet (*http://yalciner.ce.metu.edu.tr/sumatra/survey/simulation/index.htm, http://en.wikipedia.org/wiki/2004_Indian_Ocean_earthquake;http://www.nio.org/jsp/tsunami.jsp*), it can be seen that the tsunami waves travelled from the place of origin in all directions of the Indian ocean and on reaching Srilanka and the southern tip of India, these waves turned and moved to Arabian sea. Numerical modeling have also shown (Kowalik *et al*., 2005) that the main energy lobe of maximum amplitude was directed towards Srilanka and the secondary lobe was directed to South Africa and also that large portion of Arabian Sea was in the shadow of main energy lobe. This was the reason for lower intensity that was observed along west coast of India.

In the case of usual wind waves, refraction occurs only in the shallow water, while for tsunamis, which are very long waves, refraction occurs over deep waters also. However, effects due to refraction would become prominent near the coast because of the rapid decrease of depth towards the shore. Helene and Yamashita (2006) used a simple model to understand the behavior of a tsunami in variable depths and indicated the possibility of large-scale variations in the direction of propagation of tsunami due to refraction. In the present tsunami, refraction and diffraction helped it to turn the corner around the southern end of India and cause significant damage and loss of life in the state of Kerala even though Kerala is located on the western side of Indian sub continent (Ahmet *et al*., 2005).

Topography off southwest coast of India

Detailed topography is given in the refraction diagrams. Depth contours below 50m depth are closer to coast, south of Kollam. At the same time, the gap between contours of 50 and 100m is least off Trivandrum. The 1000m contour gradually turn towards offshore south off Cherthala and reaches a distance of around 110km nearly off Azheekkal. Then it turns shoreward, reaches a distance of about 80km from shore and runs at this closer distance to nearly off the tip of peninsula. Thus area between 200m and 1000m is comparatively of gentle slope north of around Azheekkal than south of this.

Methods

Study area is given in figure 2. Computer programme by Dobson (1967) has been used to generate wave refraction diagrames. It is assumed that there is no energy loss due to bottom friction and that no energy is transmitted across the wave rays. This programme was earlier used for studying refraction

pattern along the shoreline near Cochin using climatological wind wave data (Varma., 2003). In the present study, the area bounded by latitudes 7° N -10° 30' N and longitudes 74° 30'E -78° E has been chosen and the depths at grid points separated by 9 km were extracted from hydrographic chart No: 22, corrected up to 2001, after drawing additional depth contours. For completing the grid, negative depths were given to grid points lying on land, considering an arbitrary slope. Coarse grid has been used in the study because the area included is large and also because the attempt here is to find out the gross features of refraction of tsunami waves. Variations of depth, as the wave progresses shoreward, are interpolated in the computer programme with a local grid of depths with quadratic surfaces in the neighbourhood.

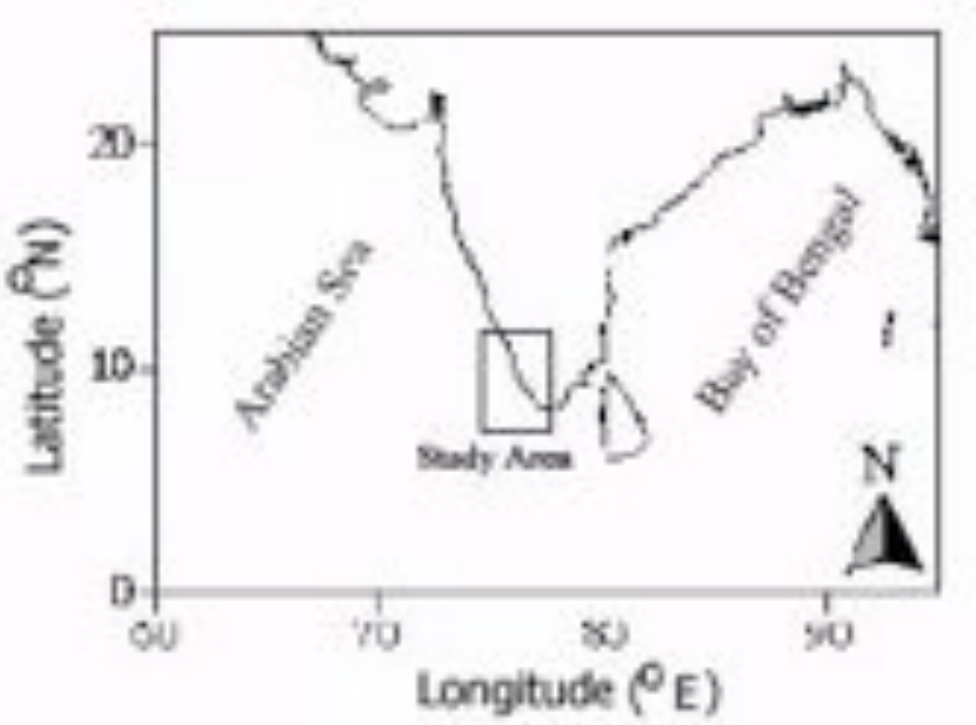

Figure 2. Study area (the rectangle indicates selected domain)

It is necessary to give a starting point of wave rays. These points are selected in such a way that these are at maximum distance from shore, that is possible within the selected domain. Initial directions that are likely to occur when these waves swing into the shadow zone are used and refraction diagrams for different wave directions of approach viz, 180, 190, 200, 210, 220, 230, 240, 250 and 260 degrees (true north), have been prepared (Fig 3 to 11).

For calculating initial velocity, the depth at the starting point is used. In other words, period of tsunami waves does not affect refraction. Since the wavelength is a requirement in the programme, the initial wavelength at the starting point of wave ray is calculated from the estimated speed, using 20 minutes as the wave period. It has been noted that the 2004 December tsunami contained different periods ranging between 20-50 minutes (Kowalik *et al*., 2005). In a recent study of the numerical modeling of tsunami waves, Paul (2006) has taken the period to be about 15 minutes. Also, on,

analyzing tide data from several places in the coastal India and neighboring places, during tsunami spectral peaks at about 20 minutes and 35-45 minutes have been noticed (Nagarajan *et al*., 2006).

Results

For180^{o}T (Fig.3) wave rays converge north of Cochin and south of Trivandrum. It can be seen that Trivandrum was a wide zone of divergence. Mild convergence was seen around Arattupuzha.

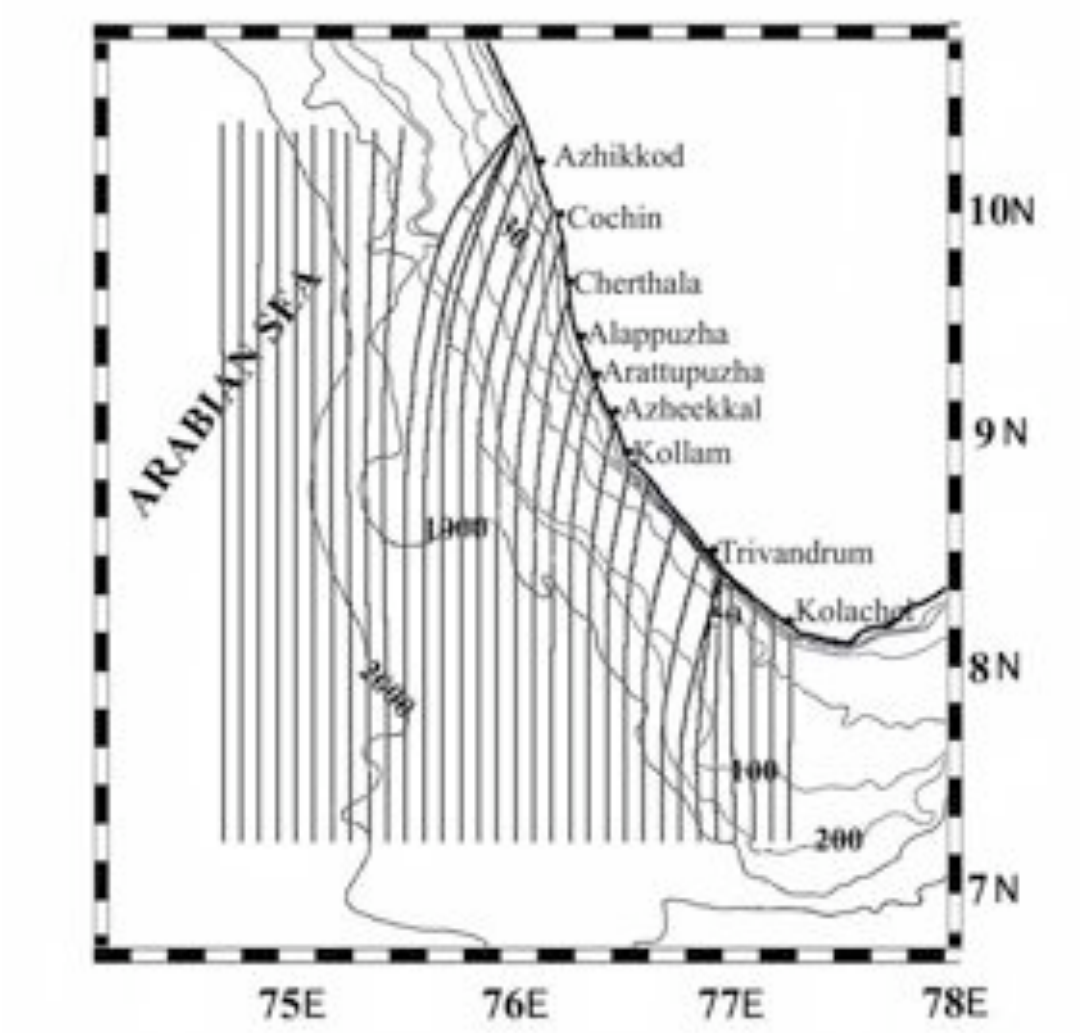

Fig.3 Refraction diagram for tsunami waves coming from 180^{o} T. Depth contours are in metres.

For 190^{o}T (Fig.4) wave rays converge around Cochin and slightly north of Kolachel. Trivandrum was in a zone of divergence. While divergence was seen at Arattupuzha, mild convergence was seen around Azheekkal. It may, however, be noted that the reported impact at Cochin was less than that at Azheekkal in Kollam area and Arattupuzha in Alappuzha zone.

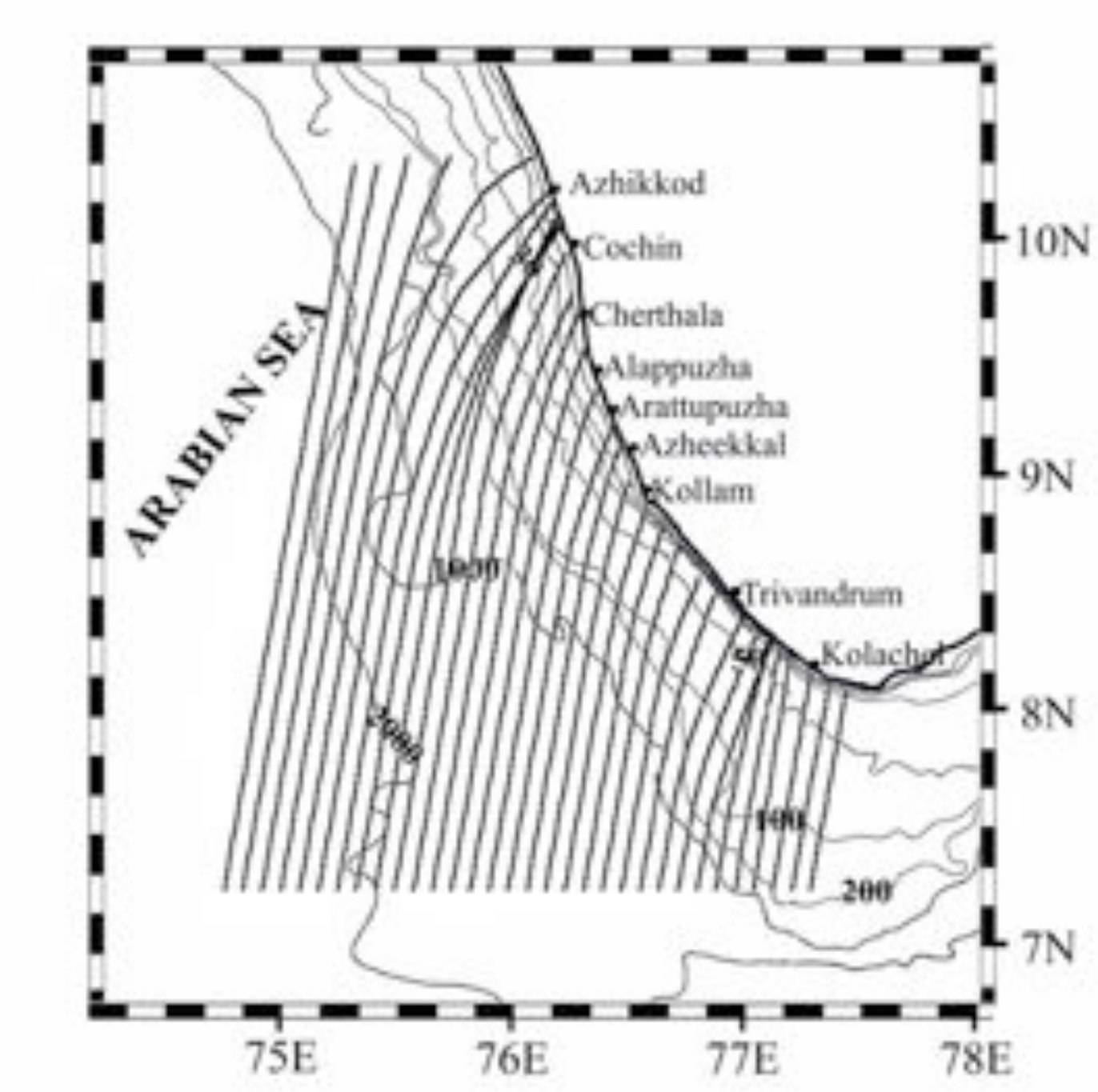

Fig.4 Refraction diagram for tsunami waves coming from 190° T. Depth contours are in metres.

For 200° T (Fig.5), the convergence zone around Cochin has moved to south and was near Cherthala. Strong convergence was seen near Kolachel. While mild convergence occurred near Azheekkal, divergence was seen at Trivandrum and Arattupuzha.

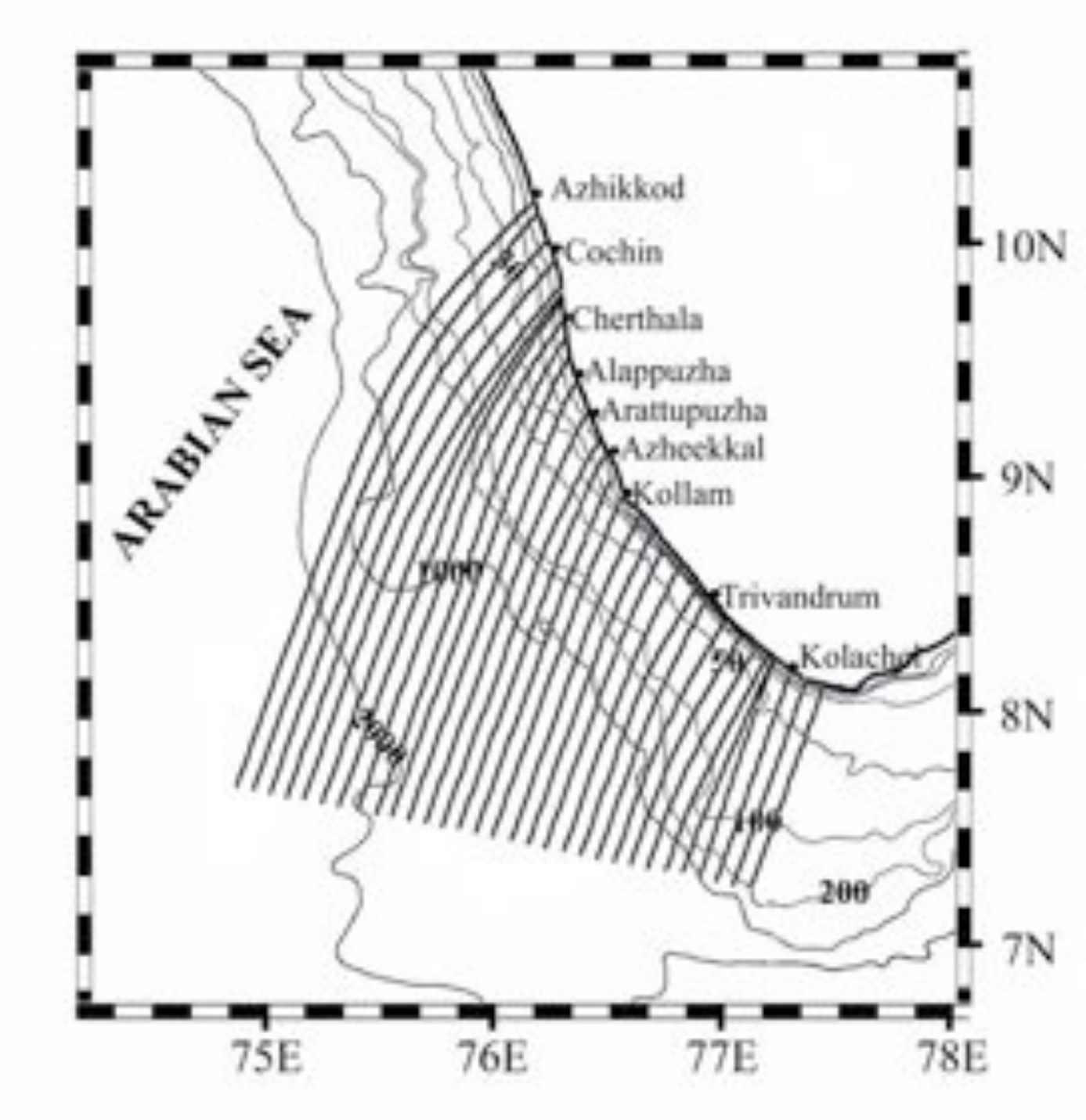

Fig.5 Refraction diagram for tsunami waves coming from 200° T. Depth contours are in metres.

In the case of 210° T (Fig.6), zones of convergence are Kolachel, Alappuzha and Kollam. Divergence was seen at Trivandrum and Arattupuzha. Mild converging tendency around Azheekkal was also seen.

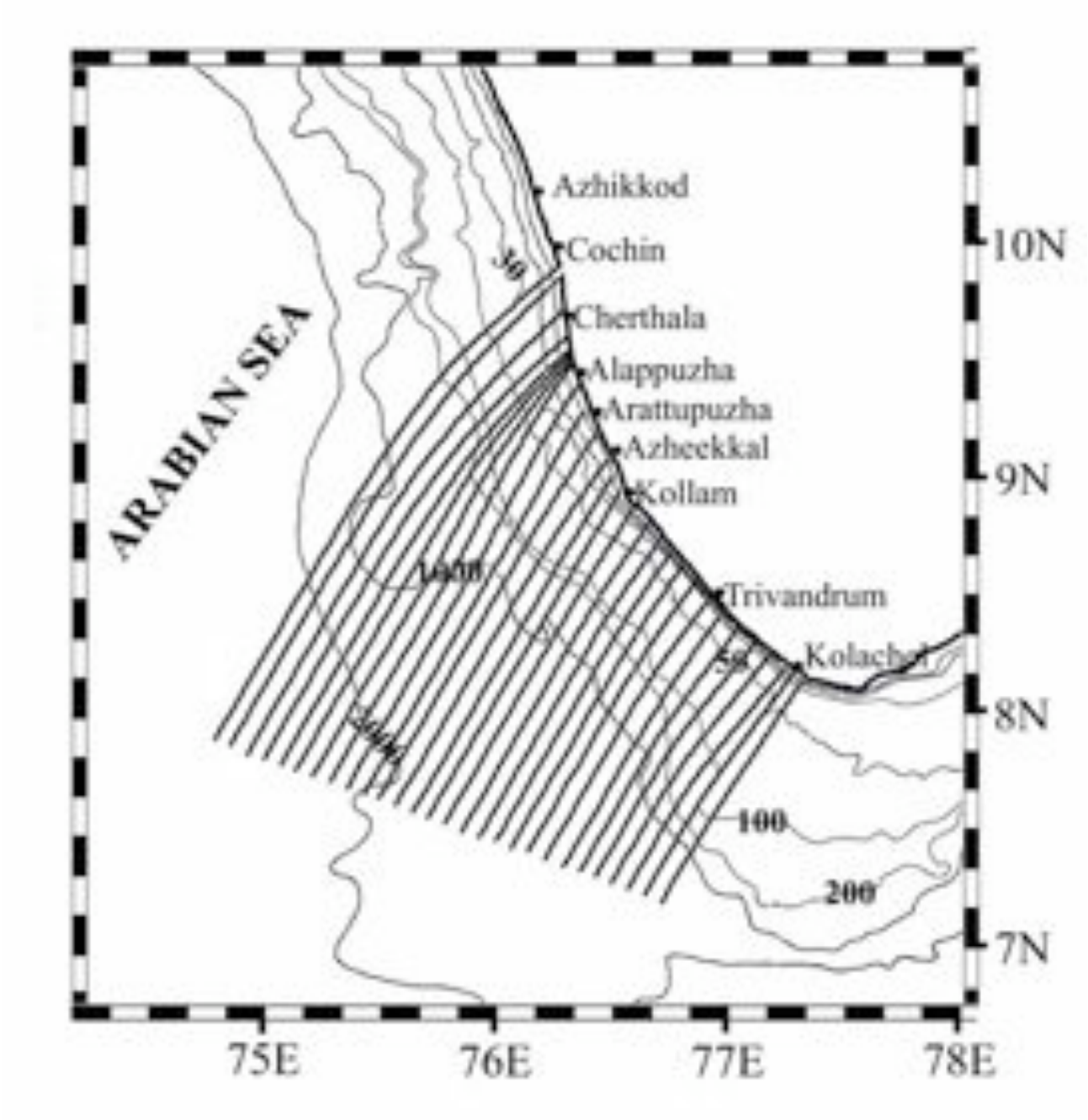

Fig.6 Refraction diagram for tsunami waves coming from 210° T. Depth contours are in metres.

For 220^{o}T strong convergence was seen between Arattupuzha and Alappuzha (Fig.7). Divergence was seen between Arattupuzha and Azheekkal. Mild converging tendency was seen near Kollam and north of Trivandrum.

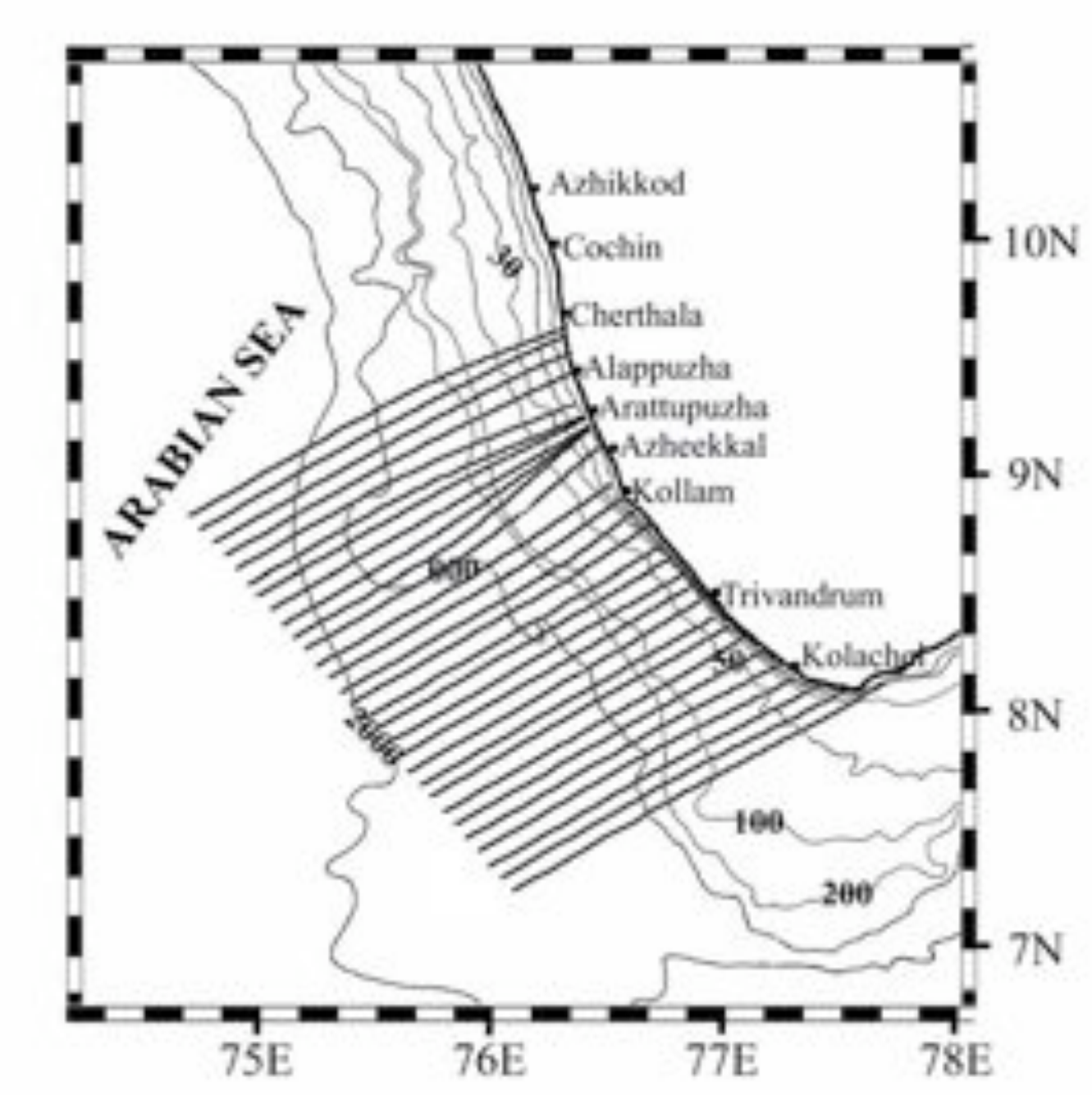

Fig.7 Refraction diagram for tsunami waves coming from 220^{o}T. Depth contours are in metres.

Directions 230° to 240° T show convergence in the Alappuzha –Arattupuzha region. Interestingly Azheekkal and Kollam were in the divergence zone (Fig 8 & 9).

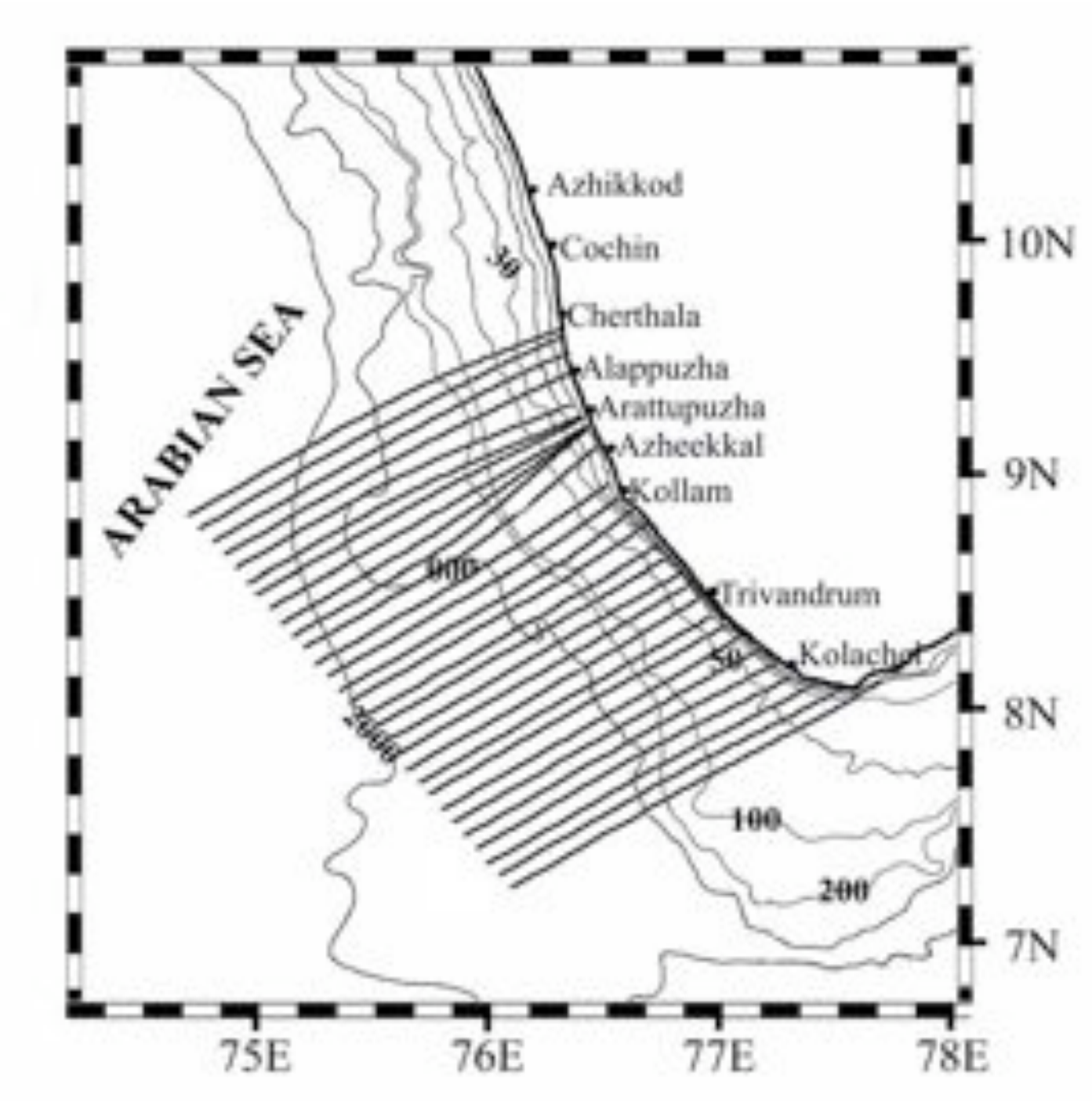

Fig.8 Refraction diagram for tsunami waves coming from 230° T. Depth contours are in metres.

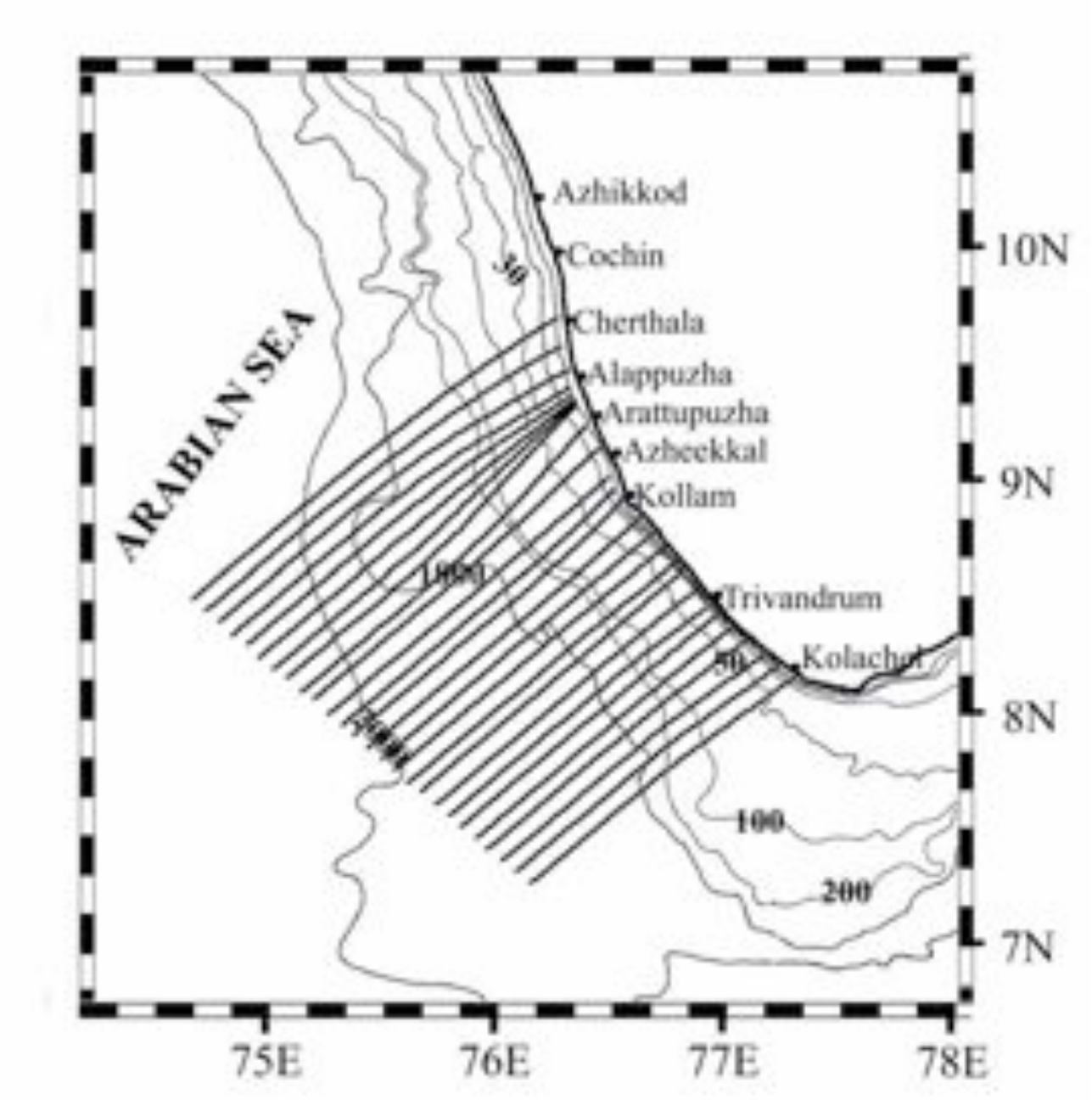

Fig.9 Refraction diagram for tsunami waves coming from 240^{o} T. Depth contours are in metres.

Though it was not sure whether more westerly directions could be there for this tsunami from Bay of Bengal, refraction diagrams for 250 and 260 were also generated (Fig 10 & 11). However, rays in the southern part only were considered because it was thought that these waves from Bay of Bengal might not swing so as to have such an approach all along the coast. For these directions convergence zones were seen in the regions of Azheekkal and Kollam.

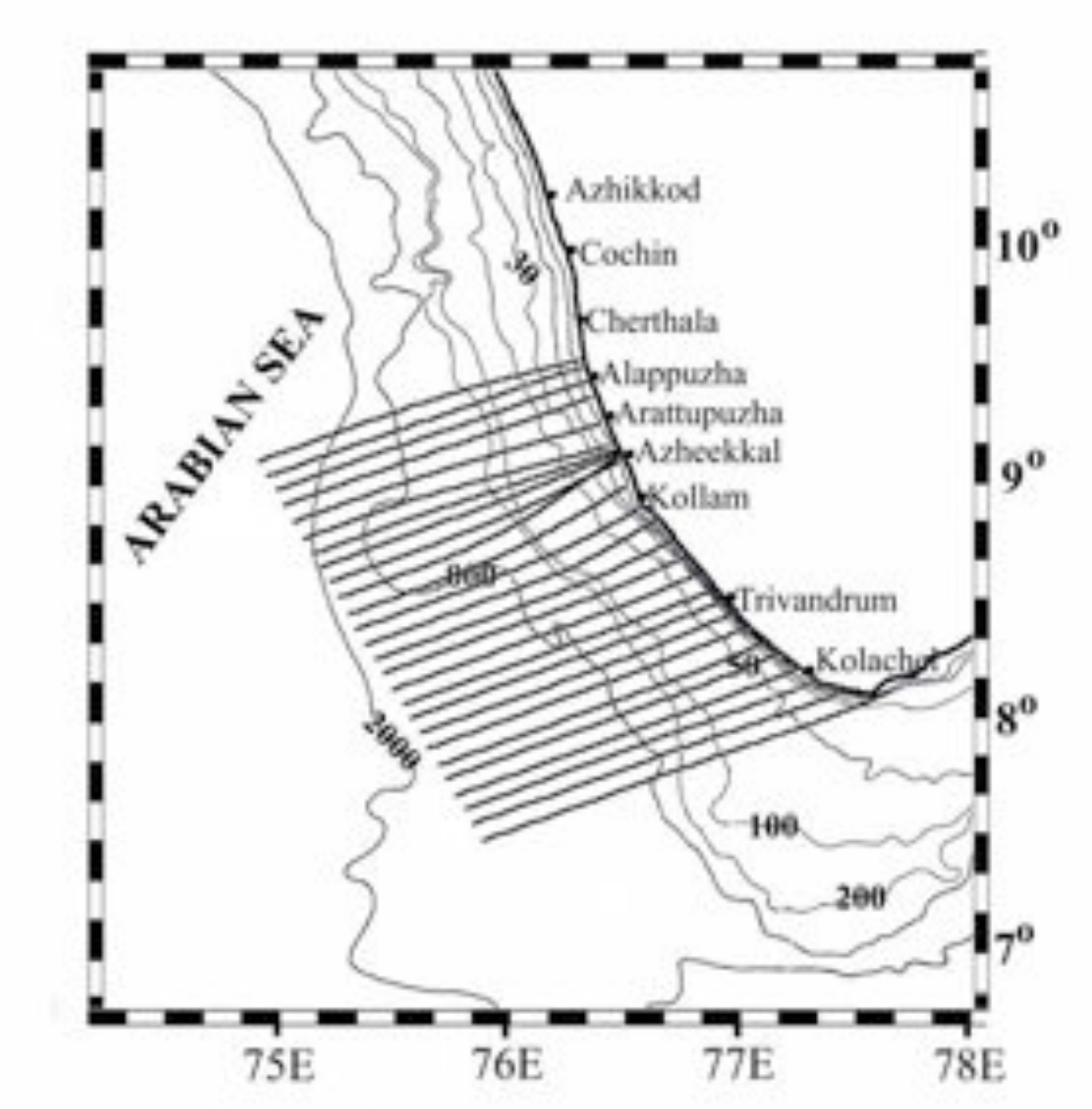

Fig.10 Refraction diagram for tsunami waves coming from 250° T. Depth contours are in metres.

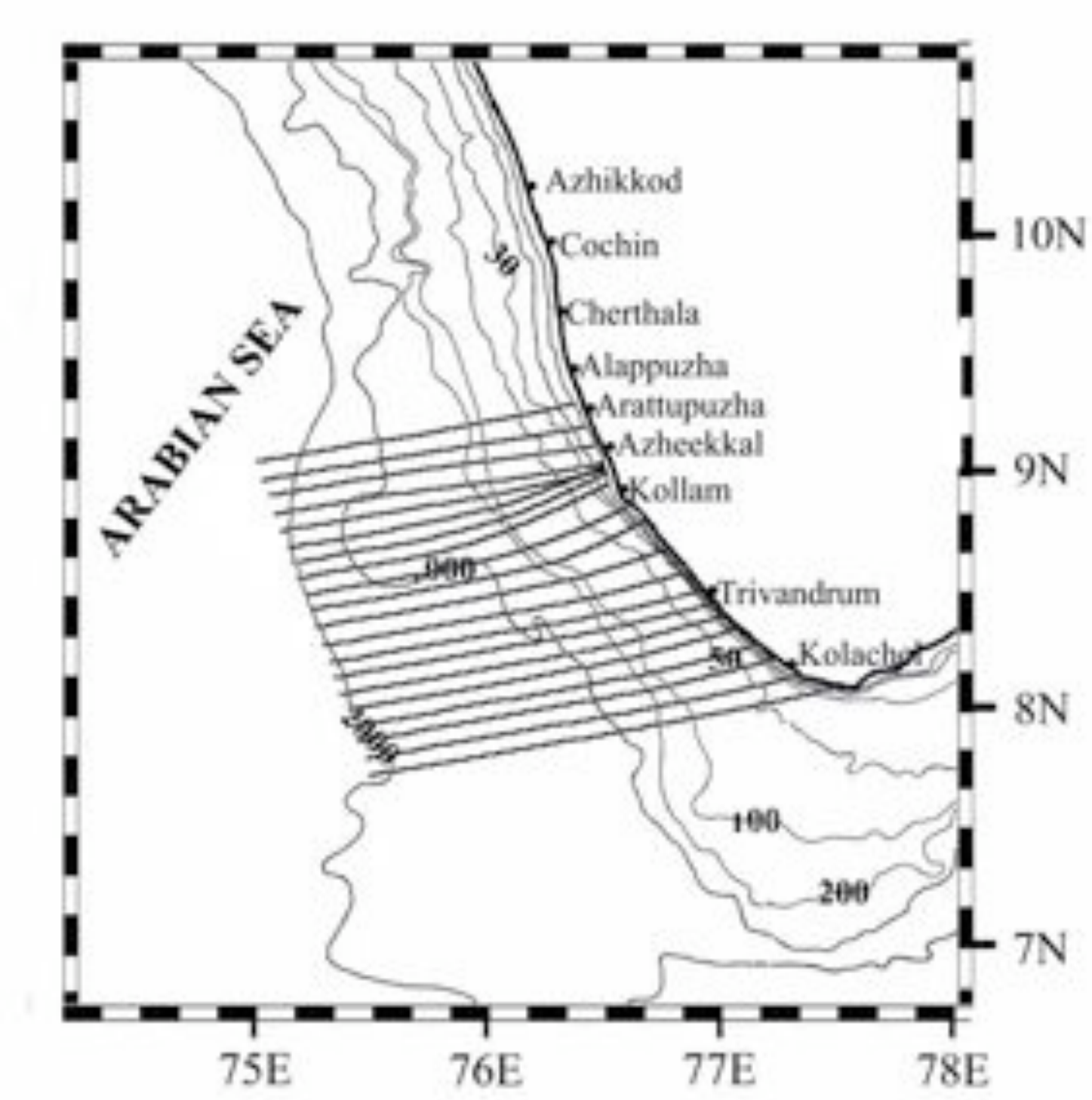

Fig.11 Refraction diagram for tsunami waves coming from 260^{o} T. Depth contours are in metres.

Discussion and conclusion

It is seen that the zones of convergence and divergence for 190° - 230° T broadly agree with the regions of destruction and those spared by the tsunami. While, areas in and around Kolachel (Kanyakumari district), Azheekkal (Kollam district) and Arattupuzha (Alappuzha district) appear as convergence zones for some directions, divergence is, generally, seen in the region between Kolachel and Kollam, which includes Trivandrum. Further westerly directions show strong convergence at Azheekkal, which is an area of higher tsunami impact. As mentioned earlier, sea bottom beyond 200m north of Azheekkal is gently sloping compared to further south**.** At the southern end comparatively wide area is seen between 500 and 1000m. Tsunamis being long waves, the refraction occurs at deeper regions itself, and the bending of waves due to north south gradient of depth several kilometers away from the coast seems to have caused the divergence around Trivandrum. The wave rays passing over the gentle off shore dome of topography around Kollam are found to cause convergence zones. This topographic feature have an influence on producing the observed impact of tsunami. While discussing about the local system of tsunami defense for Pacific coast of Kamchatka, using numerical estimates, Chubarov *et al.,* (2001) have reported that direction of tsunami movement is strictly determined by the bottom topography.

The destruction in Kolachel has been reported to be more severe, compared to other northern zones of convergence viz, around Azheekkal, around Arattupuzha and Alappuzha. In some animations available on the internet (for eg. http://news.cornell.edu/ release/Jan05/ tsunamiVid320.html), waves are seen to get reflected at Maldives Island and then impinge on southern end of the west coast of India. Thus at this zone, in addition to the convergence of energy, surges due to reflection also occurred. Refraction of such reflected waves from these islands are also to be considered. The chain of islands, Maldives, extending about 500km in north-south direction, is situated south west of the Indian peninsula. Tsunami waves, reflected from different parts of the island can possibly have some of the directions like 190° T, 200° T, 210° T and the waves with these directions are found to be favourable for convergence around Kolachel. Since reflected waves are not likely to occur in regions further northwards along the shore destructions are less severe here compared to Kolachel.

As the tsunami wave are wide, the diffraction of tsunami would have swung it in such a way that the directions over deep water could be slightly different at different parts off the west coast of India. Another aspect is that tsunamis being very long waves, they feel bottom even over deep-water oceanic areas. Hence, in present case, refraction takes place even while the wave diffracts around the land mass. It has been shown that in the case of this tsunami, refraction changed orientation to bring it to south east Arabian Sea (Helene and Yamashita., 2006). Thus different directions of approach towards the shore in the study area are possible. This could be the reason why combinations of directions ranging from 190° T to 240° T generally reproduced the broad areas tsunami impact along this coast.

Refraction diagrams along the southwest coast of India for tsunami waves have been generated, starting the wave rays from depths exceeding 1000m. Areas of convergence and divergence for

directions ranging from 190^{o}T to 240^{o}T in general agree with pattern of observed tsunami impact. Areas around Kolachel, Kollam and Alappuzha appears to be more vulnerable for tsunami generated in Bay of Bengal. Trivandrum being in the area of divergence, here the tsunami impact is likely to be less.

REFERENCES

Ahmet C.Y., Efim N.P., Ugur K., Tuncay T., Andrey S., Gulizar O., Ceren O., Hulya K., and Ilgar S., 2005. Simulation and comparison with field survey results of Dec., 26,2004-Tsunami, (*http://yalciner.ce.metu.tr/sumatra/survey/simulation/index.htm.)*

Chadha,R.K., Latha, H. Y. G., Peterson, C. and Thoshima K., 2005. The tsunami of the great Sumatra earthquake of M 9.0 on 26 December 2004 – Impact on the east coast of India. *Current Science*, 88: 1297-1301.

Chubarov,L.B., and Yu.I.S., 2001. Computational technology for constructing tsunami local warning systems, *Science of Tsunami Hazards*, 19: 23-38.

Chubarov,L.B., and Yu.I.Shokin., Computational technology for constructing tsunami local warning systems, *Science of Tsunami Hazards*, 2001, **19**, 23-38

Dobson, R.S., 1967. Some applications of a digital computer to hydraulic engineering problems, Dept of Civil Engg., Stanford Univ. *, Tech. Rep*., 80: 115.

Helene O., and Yamashita M.T., 2006. Understanding the tsunami with a simple model, *European Journal of Physics*, ,27: 855-863.

Javed, N. M., and Murthy, C.V.R., 2005. Landscape changes in Andaman and Nicobar islands (India) due to Mw 9.3 tsunamigenic Sumatra earthquake of 26 December 2004. *Current Science*, 88: 1384 1386.

Kowalik, Z., William K., Tom L., Paul W., 2005. Numerical modelling of the global tsunami, Indonesian tsunami of 26 December 2004, *Science of Tsunami Hazards*, 23: 40 – 56.

Lay T., Kanamori H., Ammon C. J., Nettles M., Ward S. N., Aster R. C., Beck S. L., Bilek S. L., Brudzinki M. R., Butler R., Deshon H. R., Ekstorm G., Satake K., and Spikin S., 2005. The great Sumtra-Andaman earth quake of 26 December 2004. *Science,* 308: 1127-1133.

Nagarajan B., Suresh I., Sundar D., Lal.A.K., Neetu S., Shenoi S.S.C., Shetye S.R., and Shankar D., 2006. The Great Tsunami of 26 December 2004: A description based on tide-gauge data from the Indian subcontinent and surrounding areas. *Earth Planet Space*, 58: 211-215.

Neetu S., Suresh I., Shankar R., Shankar D., Shenoi S S C., Shetye S.R., Sundar D and Nagarajan., 2005. *Comment on the great Sumatra-Andaman earth quake of December 26, 2004*. Science, 310: 1431a.

Paul C. Rivera, 2006, Modeling the Asian tsunami evolution and propagation with a new generation mechanism and a non-linear dispersive wave model, *Science of Tsunami Hazards*, Vol. 25, Page 18 33.

Varma K.K and Sakkeer H. A., 2005. Refraction of tsunami waves of 26th December 2004 along Kerala coast – Preliminary results, *Proceedings of Oceanographic features of Indian coastal waters*, NPOL, 73-77.

Varma K.K., 2003. Wave refraction along shoreline near Kochi, Kerala. *In science, technology, coastal zone management and policy,* (ed. Pranav N. Desai and Radhakrishanan K.V), Allied Publishers, New Delhi, 36-46.

THE ALL-SOURCE GREEN'S FUNCTION AND ITS APPLICATIONS TO TSUNAMI PROBLEMS

ZHIGANG XU

CANADIAN HYDROGRAPHIC SERVICE, MAURICE LAMONTAGNE INSTITUTE
FISHERIES AND OCEANS CANADA

P.O. Box 1000, 850 route de la Mer Mont-Joli, Québec Canada G5H 3Z4

E-mail: xuz@dfo-mpo.gc.ca

ABSTRACT

The classical Green's function provides the global linear response to impulse forcing at a particular source location. It is a type of one-source-all-receiver Green's function. This paper presents a new type of Green's function, referred to as the all-source-one-receiver, or for short the all-source Green's function (ASGF), in which the solution at a point of interest (POI) can be written in terms of global forcing without requiring the solution at other locations. The ASGF is particularly applicable to tsunami problems. The response to forcing anywhere in the global ocean can be determined within a few seconds on an ordinary personal computer or on a web server. The ASGF also brings in two new types of tsunami charts, one for the arrival time and the second for the gain, without assuming the location of the epicenter or reversibility of the tsunami travel path. Thus it provides a useful tool for tsunami hazard preparedness and to rapidly calculate the real-time responses at selected POIs for a tsunami generated anywhere in the world's oceans.

Keywords: all-source Green's functions, real-time tsunami arrival simulations, tsunami arrival time charts, tsunami gain charts.

1. INTRODUCTION

Linear long wave dynamics can adequately describe tsunami propagation in the deep ocean (> 50m, Shuto 1991). For a linear dynamic system, the Green's function, defined as the system response to isolated and impulse external forcing, is fundamental. This is because any other type of external forcing can be represented as a sum of isolated impulses and, because of the linear superposition principle, the system response to arbitrary forcing is then merely a linear combination of the Green's functions. The Green's function can be pre-calculated for fixed physical parameters and geometry of the system. The pre-calculation implies a great time saving, which is essential when a catastrophe occurs and a rapid solution is required.

Due to the complexity of realistic systems, the Green's function for most problems of interest requires numerical calculation. Since impulse forcing at one time step is equivalent to an initial condition at the next time step, a Green's function is traditionally obtained by setting up a unitary initial condition at a model grid point (source point) and then running a linearized model to get a solution field defined everywhere. This is a type of one-source-all-receiver Green's function, or briefly, one-source Green's function.

Since external forcing may happen anywhere and with any spatial distribution, one would have to run the model repeatedly by taking every grid point successively as the source point to achieve thorough hazard preparedness. If there are N grid points in total, and if one defines a run for one-source-all-receiver as a $1 \times N$ problem, then the total of all runs will be an $N \times N$ problem, which is infeasible to tackle when N is large. Consequently, such repeated runs must be limited to pre-assumed source regions, e.g., a seismic active zone (a limited-source Green's function approach).

This paper presents a new type of Green's function, an all-source-one-receiver Green's function. For convenience, it may be alternatively referred as an all-source Green's function (ASGF). The ASGF focuses on a receiver point, regarding all the model grid points as the potential sources. One may freely choose a point of interest (POI), for socio-economic, academic, or monitorial reasons, as a receiver. A run for N-sources *vs.* 1-receiver is an $N \times 1$ problem and, as will be shown in the next section, its computational cost is the same as for the $1 \times N$ problem mentioned above.

The ASGF can be used as a tool to rapidly provide responses at one or several POIs for the full range of possible tsunami source locations; it allows almost instantaneous (within a few seconds) determination of the linear response at one or several POIs to a tsunami originating anywhere in an ocean basin or even in the global ocean. We shall see that it also invites the introduction of two new types of tsunami charts, one specifying the arrival time and the other specifying the gain, without assuming the location of an epicenter or the reversibility in the travel path of a tsunami. The next section will give the basic algorithm and the mathematical definition of the ASGF. Its potential application to the tsunami problem is illustrated in Section 3 and closing remarks are given in Section 4.

2. THE ALL-SOURCE GREEN'S FUNCTION (ASGF)

For a linear system, one can write the evolution equation for its state vector, X, in the general form

$$X^{(k)} = \mathbf{A} X^{(k-1)} + \mathbf{B} F^{(k-1)} \qquad (1)$$

where $k = 1, 2, 3, \cdots$, indicate the time steps, **A** is the system matrix which encapsulates the model physics, **B** is the input matrix which projects the external forcing vector, F, onto the state vector. Once a tsunami is initiated by an earthquake or a submarine landslide, its evolution is determined by free wave propagation. This paper has two purposes, to introduce the ASGF and to demonstrate its usefulness to tsunami problems. For these purposes, the external forcing term will not be required; therefore, only the free motion problem is considered here. However, it is worth noting that the ASGF could also be used for a forced motion problem, e.g., a storm surge; in that case, continuous forcing must be considered and the second term would require additional consideration. The application of the ASGF to a storm surge problem will be considered in a future paper.

With the second term omitted, Eq. (1) can be re-expressed as

$$X^{(k)} = \mathbf{A}^k X^{(0)} \qquad (2)$$

where $X^{(0)}$ is the initial state vector, $\mathbf{A}^k$ represents the *kth* power of the system matrix (in this paper, a superscript k refers to a time step if enclosed in parentheses and to a power otherwise). Eq. (1) (without the second term) and eq. (2) are mathematically equivalent, but can differ dramatically in their computational loads. If the solutions at all model grid points are required, eq. (1) would be the choice for computational efficiency, since each time step only involves a multiplication of a matrix with a vector. In this case, to choose eq. (2) would be unwise, since, when $k \geq 2$, it would involve calculating all the *kth* powers of the whole $N \times N$ matrix **A**, which would be very expensive or infeasible when N is large. On the other hand, if only a few elements of the state vector X need to be determined (i.e., only a few model grid points are interested for having solutions), eq. (2) provides a distinct advantage as shown below.

Assume that there is only one point, say the *ith* point, where the solution is required. From eq. (2), one can write the solution at the *ith* point as

$$X^{(k)}(i) = \mathbf{A}^k(i,:) X^{(0)} \qquad (3)$$

where $\mathbf{A}^k(i,:)$ represents the *ith* row of the *kth* power of the system matrix, and the colon indicates all the columns of the matrix. The crux here is how to calculate $\mathbf{A}^k(i,:)$ economically. If one first calculates the whole matrix power, $\mathbf{A}^k$, and then extracts the *ith* row from it, the calculation is too expensive computationally. Can one obtain the value of just the *ith* row of the matrix power without calculating the other rows? The answer follows easily once the question is posed in this form. In fact,

$$G^{(1)} \equiv \mathbf{A}(i,:) \tag{4}$$

$$G^{(2)} = G^{(1)}\mathbf{A} \tag{5}$$

$$G^{(3)} = G^{(2)}\mathbf{A} \tag{6}$$

$$\vdots$$

$$G^{(k)} = G^{(k-1)}\mathbf{A} \tag{7}$$

$$\vdots$$

$$G^{(K)} = G^{(K-1)}\mathbf{A} \tag{8}$$

where the capital K represents the total number of time steps, $G^{(1)}$ is simply the *ith* row of matrix $\mathbf{A}$, and $G^{(k)}$ ($k=2,3,\cdots K$) are obtained by a series of multiplications of a row vector with the same matrix. As one can verify, $G^{(k)}$ is the *ith* row of $\mathbf{A}^k$ ($k=2,3,\cdots K$) but it is not extracted from the whole matrix to the *kth* power; it is calculated economically. The effects on the *ith* point of the coupling by all the other model grid points, as well as of the global topography and lateral boundaries, have been actually realized in the above vector-matrix multiplication sequence.

The series of $G^{(k)}$ define the ASGF, evaluated at $t = k\Delta t$ ($k=1,2,3,\cdots K$). Each $G^{(k)}$ is a row vector with N columns, each of which can be viewed as an information channel. Having N channels means that a receiver can simultaneously receive signals from N different sources without interference (think of $G^{(k)} = G^{(k)}\mathbf{I}$ where the identical matrix $\mathbf{I}$ contains N unitary sources); linearity will allow these individual contributions to be summed to obtain the full solution when required.

If we now form a new matrix $\mathbf{G}$ from the row vectors $G^{(k)}$ ($k=1,2,3,\cdots K$) as

$$\mathbf{G} = \begin{bmatrix} G^{(1)} \\ G^{(2)} \\ \vdots \\ G^{(k)} \\ \vdots \\ G^{(K)} \end{bmatrix} \tag{9}$$

then $\mathbf{G} \times X^{(0)}$ provides the solution time series at grid point i in response to an initial setup anywhere in the model domain. For a different initial setup, say, corresponding to a new tsunami, one can simply substitute a new column vector for $X^{(0)}$, without modifying the matrix $\mathbf{G}$. That is, once $\mathbf{G}$ has been determined, it can be repeatedly used; the evolution from any specified initial state is easily calculated from a simple matrix-vector multiplication. The determination of the matrix $\mathbf{G}$ may require significant computer resources, but the matrix-vector multiplication can be quickly performed even on an ordinary personal computer or on a web server.

The calculation of the aforementioned one-source-all-receiver Green's function will consist of a sequence of multiplications of the same matrix $\mathbf{A}$ and a column vector, which costs the same computationally as to calculate an all-source-one-receiver Green's function.

The ASGF approach does not require use of a particular model. All required is that the model dynamics are linear. Thus, one can always choose a better model. The ASGF will not alter the realism or quality of the particular model that it uses; it simply provides a very efficient means to quickly compute responses at particular POIs.

3. APPLICATION TO TSUNAMI PROBLEMS

This section will explore two aspects of the applications of the ASGF to tsunami problems, the real-time simulation for tsunami propagation, and two new types of tsunami prediction charts. For these applications, Heaps' two dimensional numerical sea model in spherical coordinates (Heaps 1969) is used, but rewritten in a matrix format so that the system matrix, $\mathbf{A}$, can be easily produced. The model spatial resolution is 5 min in both longitudinal and latitudinal, and the model topography is determined from a decimation of the Etopo 2 bathymetric data (http://www.ngdc.noaa.gov/mgg/fliers/01mgg04.html).

The examples presented here are influenced by artificial closed boundaries along 100^{o} W, the prime meridian, the equator and 80^{o} N. In addition, no tuning was done to improve the prediction skill of the model (e.g., by modifying friction parameters). Such improvements should clearly be implemented for practical applications, but for the demonstration purpose here, they are not essential.

3.1. Real-time tsunami propagation simulation

It is conceptually useful to think of the life of a tsunami as consisting of three phases: the genesis, the open-ocean propagation and the final onshore run-up. While the initial genesis and the final run-up are clearly nonlinear processes, the propagation through deep water fortunately obeys simple linear long wave dynamics. Nevertheless, real-time simulations for tsunami propagation are still lacking (Paul Whitmore, personal communication, 2005), principally because tsunamis move very quickly (~700 km/hour) across very large (transoceanic) domains. Even with a supercomputer and massively parallel computations, it is very difficult to win the race for time against a fast moving tsunami. The limited-source Green's function approach can provide results very quickly, but unfortunately only for cases in which a tsunami originates within source regions that are determined a priori.

The ASGF offers a new tool to address this challenge. Because it can be pre-calculated with the entire domain as potential source locations, when a tsunami-triggering event occurs anywhere within the domain, the part of the pre-calculated ASGF corresponding to the source region can be loaded into RAM, and its multiplication with the source function can yield almost instantaneously the tsunami arrival curves at one or several POIs.

Figure 1 and Figure 2 illustrate results from an R&D version of an internet-based real-time tsunami simulation system, accessible at http://odylab.qc.dfo-mpo.gc.ca . Figure 1 illustrates the graphical user interface provided in the form of a map on which one can create an arbitrary polygon defining the tsunami source region using a simple point and click procedure. Once this source region

is specified, one has the option of checking one or several points of interest where a response time series is desired. Pressing the "Make plot" button then produces the required time series within a few seconds. For the example presented here, a 100 km × 100 km square was created at the position shown by the tiny white square near x=-4000 km and y=2000 km on Figure 1. Within 6 seconds of this source specification, a pop-up window showed the response curve at Halifax (Figure 2).

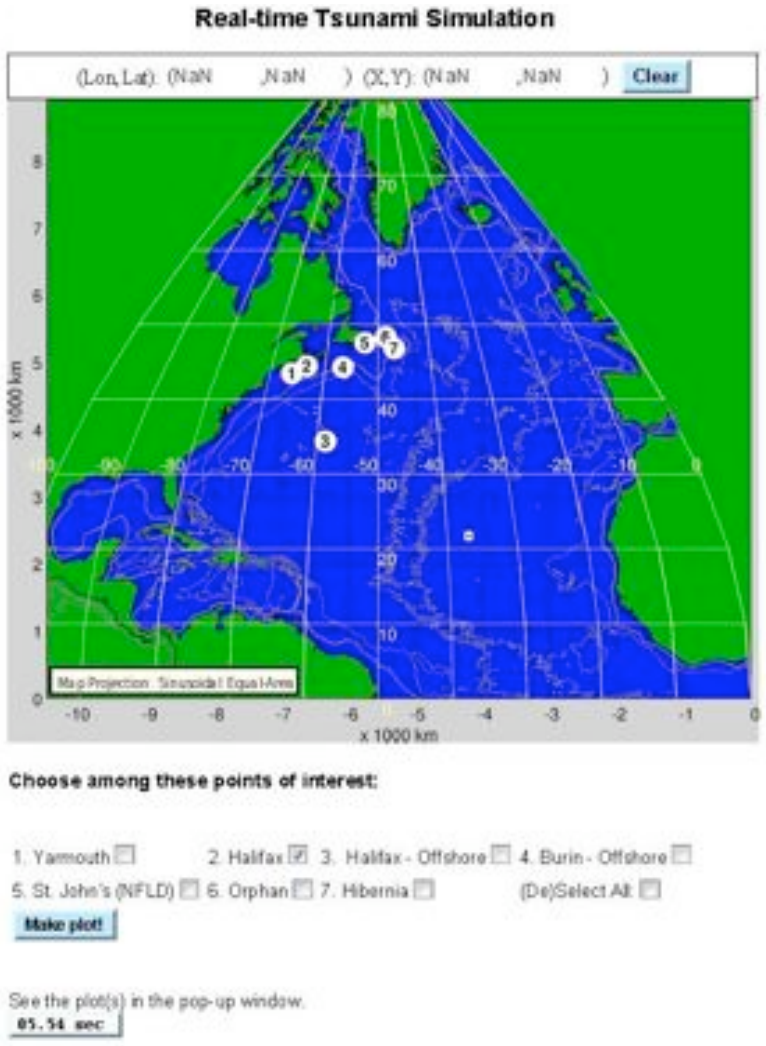

Figure 1. The graphical user interface for the tsunami simulation system. One may select points anywhere on the map to create a polygon defining the source region and then check one or more boxes as points of interest. Pressing the "Make plot" button then provides results such as those shown in Figure 2. A sinusoidal equal area map projection with a reference longitude of 50^{o} W has been used.

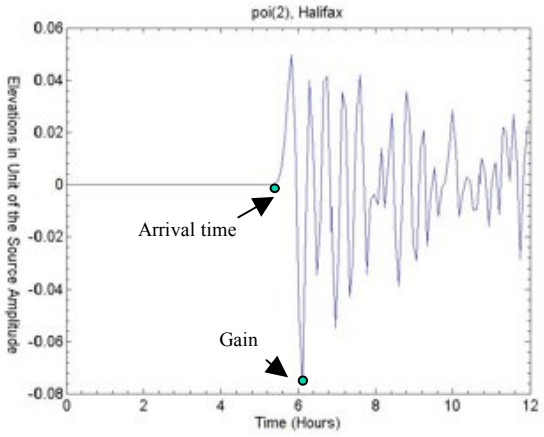

Figure 2. The tsunami arrival curve for the point of interest and the forcing region specified by the procedure described in the caption of Figure 1. Two pieces of information are particularly important, the first arrival time and the relative maximum amplitude.

3.2. New types of tsunami charts, the arrival time and the gain charts

As noted in Figure 2, two particularly useful pieces of information can be extracted from the response time series, the first arrival time of the signal and the largest relative amplitude during a certain period. The largest relative amplitude is defined as a gain since it is relative to the source unit. Proper definitions of the arrival time and gain can be discussed later. For demonstration purposes here, the arrival time is defined as the first time when a signal with 1/1000 relative amplitude (positive or negative) arrives, and a period of 12 hours is taken within which the maximum absolute relative amplitude is searched to determine the gain.

The 100 km × 100 km square in Figure 1 was purposefully chosen so that one can use it to tile the model domain. Each of the tiles will then give a pair of numbers for the arrival time and the gain. Contouring them gives an arrival time chart and a gain chart. Figure 3 and Figure 4 illustrate these charts for Halifax as the POI and the North Atlantic Ocean as the source field. In Figure 3, different color bands indicate arrival times at Halifax for disturbances generated anywhere over the model domain. Any tsunami originating in the same color band would arrive at Halifax within the same hour. The gain chart, Figure 4, gives the magnitude at any source point in the domain of the largest amplitude at the POI if a unit tsunami originates from that source point. It reveals a spatial structure indicating which potential generation locations would have maximal impact on a particular POI. Both charts are equally important. A combination of the gain map with a hazard map for earthquakes and submarine landslides should provide a useful tool for tsunami risk analysis.

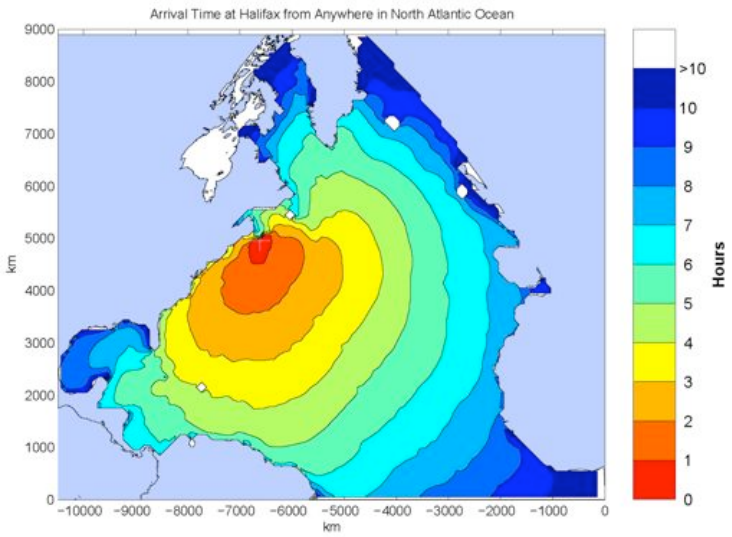

Figure 3. Arrival time map for Halifax as a POI. Any tsunami originating in the same color band would arrive at Halifax within the same hour.

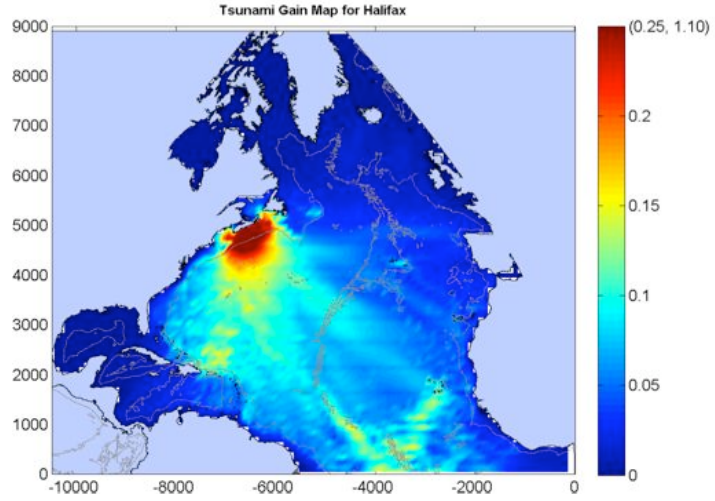

Figure 4. Gain map for Halifax. It gives the magnitude at any source point in the domain of the largest amplitude at the POI if a unit tsunami originates from that source point over a 100 km x 100 km region. It provides a spatial structure indicating which source regions would generate the largest responses at Halifax.

The tile size may, of course, be made as fine as the model spatial resolution, which is 5 min in both longitude and latitude for the model used to generate the results illustrated in this section (≈10 km x 10 km cells in the equatorial region). However, since the gain is reduced for smaller tile size, the details of the map depend on this choice. A 100 km tile, with about 144 model grid points, was chosen

here so that the gain map has both good spatial resolution and is still readable. The curve seen in Figure 2 is actually a summation of the contributions of these individual source points.

A traditional tsunami chart only contains information on the tsunami travel time, not on its amplitude. This is because it is made with an approach where a tsunami is treated as an optical ray from an assumed source. In this approach, one can deal with the time easily, but not so with the amplitude. Moreover, the usefulness of such a chart depends on whether a future tsunami will indeed originate from the assumed epicentre. To overcome this source dependence, one must also assume that a tsunami travel path is reversible like a light ray path and hence if one switches the source and receiver positions, the travel time is still the same. This reversibility assumption allows one to interpret the travel time from a POI to anywhere in the domain as the arrival time from anywhere to the POI, whereas the former can be obtained by placing a source simply at the POI and using the ray tracing technique. It has been the practice to use the ray tracing technique and the path reversibility assumption for making the tsunami charts (Paul Whitmore, 2006 and Tad S. Murty, 2006, personal communications; also see http://slowmo.sourceforge.net/).

It will be interesting to see how valid this path reversibility assumption is. On the one hand, we all know that the geostrophic component of long waves in the ocean prefer certain directions for their travel. For example, under the effect of the earth's rotation, they tend to travel in a direction with the shallow water to their right (left) hand side in the northern (southern) hemisphere (e.g., Pedlosky 1979). However, the purpose of this paper is not to conduct an expanded discussion on the path reversibility.

The arrival time and the gain charts made with the ASGF do not assume specific epicentres or the path reversibility. The Coriolis effect, the seabed frictional effects, and the wave refractions and reflections caused by arbitrary coastlines and topography are all accounted for.

4. CLOSING REMARKS

The all-source Green's function has been defined and an algorithm for its determination has been provided. Its usefulness in tsunami problems also has been demonstrated; it makes real-time simulation feasible and it introduces the arrival time and gain charts without assumptions about the epicentre location or the reversibility of tsunami ray paths.

In comparison with the traditional one-source-all-receiver Green's functions, the all-source-one-receiver Green's function has the following advantages: 1) The latter covers source points for the entire model domain whereas the former only covers one source point. 2) POIs are more easily identified than potential source regions; one may use a thousand POIs to cover comprehensively the important coastal cities worldwide, and perhaps a dozen POIs for an island country or region. In contrast, model grid points can easily number in the millions. To cover m POIs, the latter approach results in an $m \times N$ problem which is still linear in N (as long as $m \ll N$) and can be easily handled by modern computers.

The index i was taken to indicate a single POI in the discussion of the numerical algorithm, this was just for simplicity of presentation; nothing prevents use of the index i to represent several distinct POIs. One can thus use the same algorithm to calculate the ASGFs for several POIs simultaneously.

Also, the algorithm is completely ready for parallel computation; one can assign values of i to different processors or even different computational platforms and compute the individual solutions without any need for exchange of information between processors. It should be feasible to calculate and store the ASGFs for worldwide important cities as POIs and the entire global ocean as the potential sources. It would also be interesting to make a tsunami atlas consisting of the arrival time and gain charts covering the global domain.

The system matrix, A, should be very sparse, since it results from discretization of a set of partial differential equations. The Heaps's model adopted in this paper gives a sparsity of the order of 10^{-6} (the ratio of non-zero elements versus the total elements in the matrix). One should use a good sparse matrix technique, such as the nonzero-element-only technique implemented in Matlab (Gilbert *et al* 1992), for efficiency in the CPU time and in the disk storage.

The ASGF does not address the tsunami initial set-up or the final run-up issue but only addresses the tsunami propagation issue. However, it is the propagation issue that is the most computationally challenging. The ASGF provides an efficient intermediate connection between a genesis model and a run-up model at the two ends.

The initial state vector, $X^{(0)}$, contains both the elevations and the depth average velocities. This will allow for different types of initial conditions: the elevation only, or the currently only, or a mixture of them.

ACKNOWLEDGEMENTS

This work has benefited from personnel communications with Dr. Paul Whitmore and Tad S. Murty. Thorough internal reviews by Dr. Dan Wright, Brian Petrie, Denis Lefaivre and John Loder are greatly appreciated. The author also thanks Mr. Michel Beaulieu for his help in setting up the ODYLAB extranet site to demonstrate the real-time tsunami simulations. This work is partially supported by Fisheries and Oceans Canada's COMDA (Centre for Ocean Model Development and Application). It also benefits from another closely related project, Study of Water Level Variations and Modelling of Storm Surges in the Estuary and Gulf of St. Lawrence, co-funded by Canadian Foundation for Climate and Atmospheric Science and by the Québec provincial consortium URANOS on Climate Change.

REFERENCES

Gilbert J. R., Moler C., and Schreiber R. 1992. Sparse matrices in MATLAB: Design and implementation. *SIAM J. Matrix Anal. Appl.*, 13(1):333—356

Heaps. N. S. 1969. A Two-Dimensional Numerical Sea Model, *Phil. Trans. R. Soc.* A, 265, 93-137.

Pedlosky, J. 1979. Geophysical Fluid Dynamics, Springer Verlag, Berlin and New York.

Shuto N. 1991. Numerical Simulation of Tsunamis --- Its Present and Near Future. *Natural Hazards* 4: 171-191.

Science of Tsunami Hazards, Vol 26, No. 1 (2007) ISSN 8755-6839

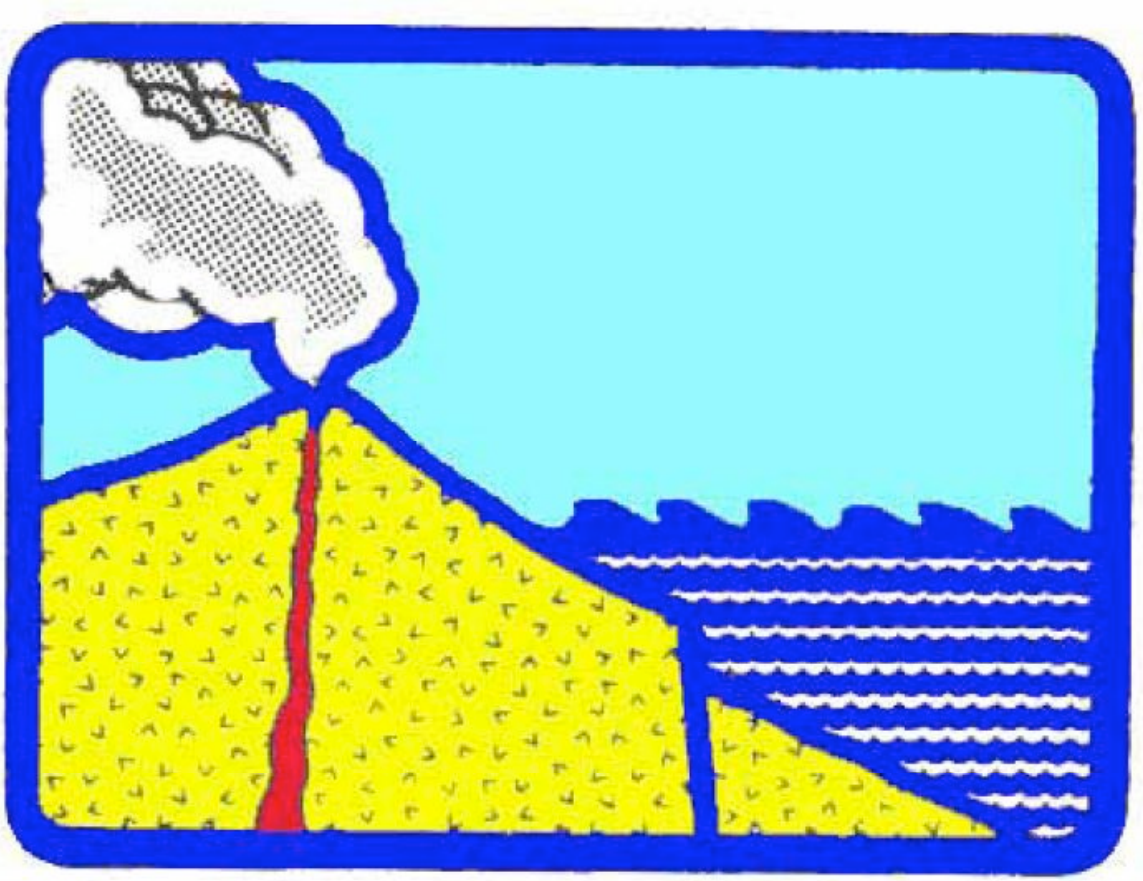

The Tsunami Society
P. O. Box 2117
Ewa Beach, HI 96706-0117, USA

WWW.TSUNAMISOCIETY.ORG